

# The Formation of Disc Galaxies

M.L. Weil,<sup>1,2</sup> V.R. Eke,<sup>1,3</sup> and G. Efstathiou<sup>1,3</sup>

<sup>1</sup>*Department of Physics, Oxford University, Astrophysics Building, Keble Road, Oxford OX1 3RH*

<sup>2</sup>*Astronomy Department, Columbia University, New York, NY*

<sup>3</sup>*Institute of Astronomy, Madingley Road, Cambridge CB3 0HA.*

27 August 2021

## ABSTRACT

We investigate the influence of the cooling epoch on the formation of galaxies in a cold dark matter dominated universe. Isolated haloes, with circular speeds typical of spiral galaxies, have been selected from a low resolution numerical simulation for re-simulation at higher resolution. Initial conditions for each halo consist of a high resolution region containing dark matter and gas, and a nested hierarchy of particles representing the mass distribution of the original low resolution simulation. These initial conditions are evolved with two smoothed particle hydrodynamics (SPH) codes, TREESPH and GRAPESPH, so that discrepancies due to differences in evolutionary and star formation algorithms can be analysed. In previous SPH simulations, strong outward transport of angular momentum has led to the formation of disc-like systems with much smaller angular momenta than observed in real disc galaxies. Here we investigate whether this problem can be circumvented if feedback processes prevent disc formation until late epochs. In some of our models, the gas is evolved adiabatically until a specified redshift  $z_{\text{cool}}$ , at which point the gas is allowed to cool radiatively and star formation may begin. In other models, cooling is continuous throughout the evolution but suppressed by a factor chosen to allow a discs to grow roughly linearly with time. The results of varying the cooling epoch for each of five different haloes are analysed. When cooling and star formation are initiated at redshift  $z_{\text{cool}} = 4$ , stellar discs are destroyed during merger events and we observe similar catastrophic transport of angular momentum as seen in previous work. With cooling suppressed until  $z_{\text{cool}} = 1$ , discs can form by the present day with angular momenta comparable to those of observed disc galaxies. We conclude that feedback processes, which prevent gas from collapsing until late epochs, are an essential ingredient in disc galaxy formation.

## 1 INTRODUCTION

Cosmological N-body simulations have shown that the evolution of small density perturbations in an expanding universe can lead to a distribution of matter very similar to the observed large-scale structure (see *e.g.* Jenkins *et al.* 1998). Purely N-body simulations have also led to an understanding of the evolution of dark matter on the scale of individual galaxies. For example, simulations of cold dark matter (CDM) models have shown how dark matter haloes form by the hierarchical merging of sub-units (Frenk *et al.* 1988), acquire angular momentum via tidal torques (Barnes and Efstathiou 1987), and develop radially-averaged density profiles that satisfy simple scaling relations (Navarro, Frenk & White 1997).

Gas-dynamical simulations of the formation of individual galaxies within dark matter haloes have been much less successful. In simulations without star formation (*e.g.* Navarro & Steinmetz 1997), the gas component can shock and dissipate energy (unlike the collisionless halo material) forming thin discs within the dominant halo sub-clumps. The gas discs may be disrupted in subsequent mergers, but

the efficient conversion of kinetic energy to thermal energy and rapid cooling allows the gas to settle into a new disc on a timescale that is short compared to the Hubble time. The evolution thus proceeds through a hierarchy of disc formation and merging, leading, in the absence of star formation, to gaseous discs at the present day. However, during merging, angular momentum is efficiently transported outward into the halo and the resulting gaseous discs have angular momenta some two orders of magnitude below those of observed spiral galaxies (Navarro & Steinmetz 1997). Evidently, such simulations cannot account for the formation of real disc galaxies. We will sometimes refer to this problem as the ‘angular momentum catastrophe’.

On the other hand, in simulations in which efficient star formation is included, stars form within dark matter sub-clumps at early times. These largely stellar sub-units then merge as the system evolves, losing angular momentum and forming a hot spheroidal component by the present day. The final objects in such simulations are elliptical-like with no strong disc structure (*e.g.* Katz 1992).

The failure to produce realistic disc galaxies in numer-

arXiv:astro-ph/9802311v1 24 Feb 1998

ical simulations contrasts with simple analytical models of disc galaxy formation. These models, first developed by Fall and Efstathiou (1980) and Gunn (1982), show that the sizes and collapse times of disc galaxies can be understood within the context of a two-component (gas and dark matter) theory of galaxy formation (White and Rees 1978) *provided the gas component conserves its angular momentum during collapse*. More recent applications of this type of model have been developed to explain other properties of disc galaxies, *e.g.* the slope and scatter of the Tully-Fisher (1977) relation (Mo, Mao & White 1998) and the distribution of disc surface brightnesses (Dalcanton, Spergel and Summers 1997). In fact, we will show in Section 2 of this paper, that simple arguments can be developed to show that in CDM models, galactic discs cannot have lost much angular momentum during collapse. There is, therefore, an apparent inconsistency with the ‘angular momentum catastrophe’ described above.

In this paper we suggest that this conflict might be solved if stellar feedback processes prevent discs forming until late epochs ( $z \lesssim 1-2$ ). If some fraction of the protogalactic gas is prevented from collapsing until late epochs, when galactic dark matter haloes are evolving slowly and most of their substructure has been erased, then it may be possible to form discs without the angular momentum transport characteristic of merging sub-units. Our aim in this paper is to test this idea using SPH simulations.

We review the observed angular momenta of disc galaxies in Section 2 and compare them with the angular momenta of CDM haloes determined from N-body simulations. We discuss also the surface brightness distributions of disc galaxies which we relate to the large dispersion in the angular momenta of CDM haloes. The SPH codes that we use, and various other numerical details such as the star formation algorithms, are described in Section 3. The generation of initial conditions for the SPH simulations is described in Section 4 and our main results are presented in Section 5.

## 2 THE ANGULAR MOMENTA OF SPIRAL DISCS

In this section, we review observational constraints on the angular momenta of disc galaxies and compare the results with the angular momenta of dark haloes in N-body simulations of a CDM model.

We first investigate the angular momenta of haloes identified in numerical simulations of an  $\Omega = 1$  scale invariant CDM model. There have been many previous investigations of this problem, including Barnes and Efstathiou (1987), Frenk *et al.* (1988), Zurek, Quinn and Salmon (1988), and more recently by Lemson and Kauffmann (1997). The results described here are based on the simulation that is used to generate the initial conditions of the high resolution SPH simulations described in the main part of this paper. The numerical simulation used here is run (d) of the ensemble described by Efstathiou (1995). The simulation is of a spatially flat  $\Omega = 1$  CDM model with scale-free Gaussian initial conditions generated from the power spectrum given by equation

(7) of Efstathiou, Bond & White (1992) with  $\Gamma = \Omega h = 0.5^*$ . We assume  $h = 0.5$  in the rest of this paper, unless explicitly stated otherwise. The simulation contains  $N_p = 10^6$  particles within a cubical volume of box-length  $L_{\text{box}} = 40$  Mpc, with the spectrum normalized so that the rms mass fluctuations in spheres of radius  $8h^{-1}$  Mpc is  $\sigma_8 = 0.59$  at the present day. This normalization approximately matches that inferred from the abundances of rich clusters of galaxies in an  $\Omega = 1$  universe (White, Efstathiou & Frenk 1993; Eke, Cole & Frenk 1996). The mass per particle in the simulation is  $4.43 \times 10^9 M_\odot$ .

Haloes are identified by linking together particles separated by 0.2 times the mean interparticle separation using the percolation algorithm described by Davis *et al.* (1985). The mean overdensity of these haloes is  $\Delta \approx 200$ , corresponding roughly to the critical overdensity defining the virialized region of a collapsed uniform sphere. For each halo, we compute the angular momentum  $J$ , mass  $M$ , total energy  $E$  and circular speed  $v_c$  defined by

$$v_c^2 = G \frac{M(< R_c)}{R_c}, \quad (1)$$

where  $M(< R_c)$  is the mass contained within a sphere of radius  $R_c$  centred at the centre of mass of the halo. We used a radius of  $R_c = 0.4$  Mpc, which is approximately the virial radius of a halo with a circular speed of 200  $\text{kms}^{-1}$  (see equation 4). We also compute the dimensionless spin parameter  $\lambda$  (Peebles 1969)

$$\lambda = J|E|^{1/2} M^{-5/2} G^{-1}. \quad (2)$$

Fig. 1a shows the specific angular momenta for haloes identified at  $z = 0$  plotted against their circular speeds. This type of diagram is more instructive than the usual plot showing specific angular momentum against either halo or disc mass (Fall 1983, Navarro & Steinmetz 1997), because the circular speed of a collapsed, centrifugally supported disc is likely to be closely similar (to within 50%) of the halo circular speeds (see Section 5, and Mo *et al.* 1998). With a diagram such as Fig. 1, the circular speeds measured for real disc systems can be used as indicators of the circular speeds, and typical specific angular momenta, of the haloes in which they formed.

For a halo with density profile

$$\rho_H(r) = \frac{v_c^2}{4\pi G r^2}, \quad (3)$$

the virial radius is given by

$$\begin{aligned} R_H &= \left(\frac{2}{\Delta}\right)^{1/2} \frac{v_c}{H_0} (1+z)^{-3/2} \\ &= 0.3(1+z)^{-3/2} v_{300} (\Delta_{200})^{-1/2} h^{-1} \text{Mpc}, \end{aligned} \quad (4)$$

where we have assumed  $\Omega = 1$  and the notation  $v_{300} = v_c/300 \text{kms}^{-1}$ ,  $\Delta_{200} = \Delta/200$ , *etc.* If we assume that the halo density profile truncates at  $r = R_H$ , we can compute the specific angular momentum from the spin parameter  $\lambda$

$$\begin{aligned} j(R_H) &= \sqrt{2} \lambda v_c R_H \\ &\approx 6.5 \times 10^3 (1+z)^{-3/2} \lambda_{0.05} v_{300}^2 h^{-1} \text{kms}^{-1} \text{kpc}^{-1}. \end{aligned} \quad (5)$$

\* Where  $h$  is the Hubble constant in units of  $100 \text{kms}^{-1} \text{Mpc}^{-1}$  and  $\Omega$  is the cosmological density parameter.

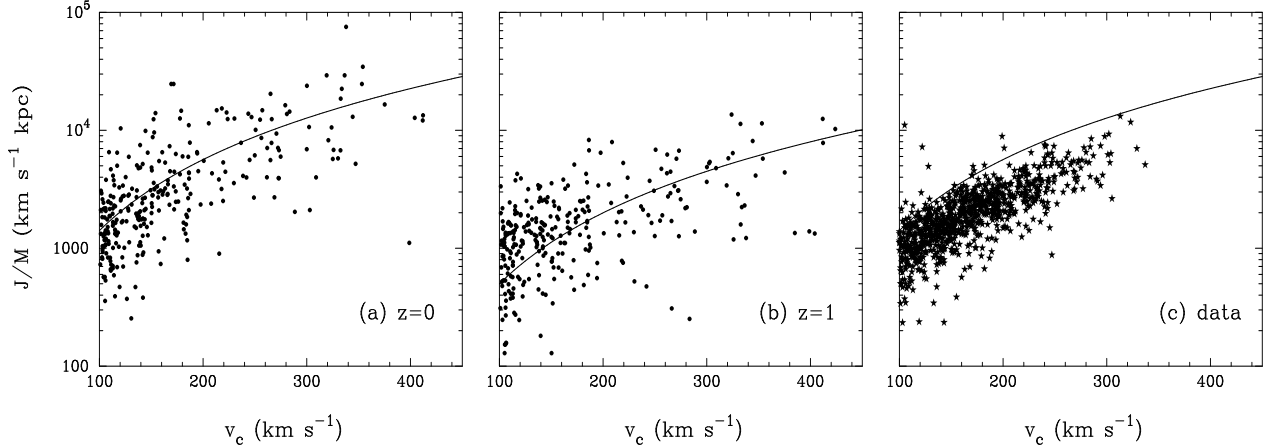


**Figure 1.** (a) The circles show the specific angular momenta of haloes with an overdensity  $\Delta \approx 200$  identified in an  $\Omega = 1$  N-body simulation of a CDM universe plotted against their circular speeds. The solid line shows the specific angular momentum expected for a halo with dimensionless spin parameter  $\lambda = 0.05$  (equation 5); (b) as (a) except that the specific angular momenta have been computed for haloes identified at  $z = 1$  and the circular speeds are those of the haloes at  $z = 0$  within which they merge. The solid line is equation 5 with  $z = 1$ ; (c) the symbols show the specific angular momenta of a sample of disc galaxies described in the text and the solid line shows equation 5 as plotted in panel (a).

where we have chosen  $\lambda = 0.05$ , since this is approximately the median value of  $\lambda$  measured for haloes in CDM models (Barnes & Efstathiou 1987). Equation 5 is shown as the solid line in Fig. 1 and provides an excellent approximation to the median specific angular momentum as a function of circular speed.

The results plotted in Fig. 1a probably provide a conservative upper limit to the angular momenta of disc galaxies. The angular momentum of the disc component will depend on the epoch at which the gas that forms the disc can cool, and on its radial extent. The specific angular momentum of discs will be lower than shown in Fig. 1a if either the disc gas collapses from well within the virial radius  $R_H$ , or if the disc collapses at high redshift. For example, Fig. 1b shows the specific angular momenta of haloes identified at  $z = 1$  plotted against the circular speed of the halo at  $z = 0$  within which they merge. The solid line in the plot shows equation 5. The specific angular momenta of haloes at  $z = 1$  are typically three times smaller than at  $z = 0$ , because the virial radius at  $z = 1$  is about three times smaller than at  $z = 0$  and haloes typically display a nearly constant rotation speed with radius (Frenk *et al.* 1988).

The third panel in Fig. 1 shows the specific angular momenta for a large sample of disc galaxies plotted against their circular speeds. The photometric parameters are from Byun & Freeman (unpublished). These authors have analysed I-band CCD images of galaxies from the Mathewson, Ford & Buchhorn (1992) sample, using a two-dimensional profile fitting algorithm described by Byun & Freeman (1995). Each image has been decomposed into  $r^{1/4}$ -law bulge and exponential disc components, providing estimates of the exponential disc scale length  $\alpha^{-1}$ , central surface brightness  $I_0$ , bulge-to-disc ratio  $B/D$ , inclination angle and I-band apparent magnitude. We use estimates of the circular speeds  $v_c$  given in Mathewson *et al.* (1992), corrected for inclination,

to compute the specific angular momenta for a centrifugally supported exponential disc with a flat rotation curve.

$$\frac{J}{M} = 2v_c\alpha^{-1}. \quad (6)$$

We assume  $H_0 = 50 \text{ km s}^{-1} \text{ Mpc}^{-1}$  to compute distances and include only galaxies with distances  $> 10 \text{ Mpc}$  and bulge-to-disc ratios  $B/D < 0.3$ , to reduce errors arising from inaccurate distances and poorly determined disc profile parameters. These selection criteria reduce the number of galaxies from 1355 in Byun & Freeman's sample to 1036. The solid line in Fig. 1c shows equation 5 with  $z = 0$  (*i.e.* as plotted in Fig. 1a). This line lies about three times higher than the median defined by the data points. This is encouraging because it shows that the angular momentum of a typical disc galaxy is similar to the angular momentum within the virialized region of a present day CDM halo of similar circular speed.

Fig. 1 also shows that the scatter in the specific angular momenta of real disc galaxies is comparable to the scatter of the specific angular momenta measured for N-body haloes. This can be demonstrated using the following simple argument (Efstathiou & Barnes 1984). Assume that a fraction  $f_D$  of the baryonic mass within the virial radius of a halo collapses to form a disc. The luminosity of the disc is

$$L_D = f_D M_H \left( \frac{L}{M} \right)_D = f_D \frac{v_c^3}{H_0 G} \left( \frac{L}{M} \right)_D \left( \frac{2}{\Delta} \right)^{1/2} \propto v_c^\alpha, \quad (7)$$

where the expression for  $M_H$  has been substituted assuming that  $\Omega = 1$  and  $z = 0$ . The proportionality expresses the tight Tully-Fisher (1977) correlation between luminosity and circular speed observed for real disc systems. Evidently, the (uncertain) cooling and feedback processes which determine  $f_D$  must be tightly correlated with circular speed to reproduce the Tully-Fisher relation. The correlation between disc luminosity and circular speed for the Byun-Freeman sample is shown in Fig. 2a. A least squares fit to the data points

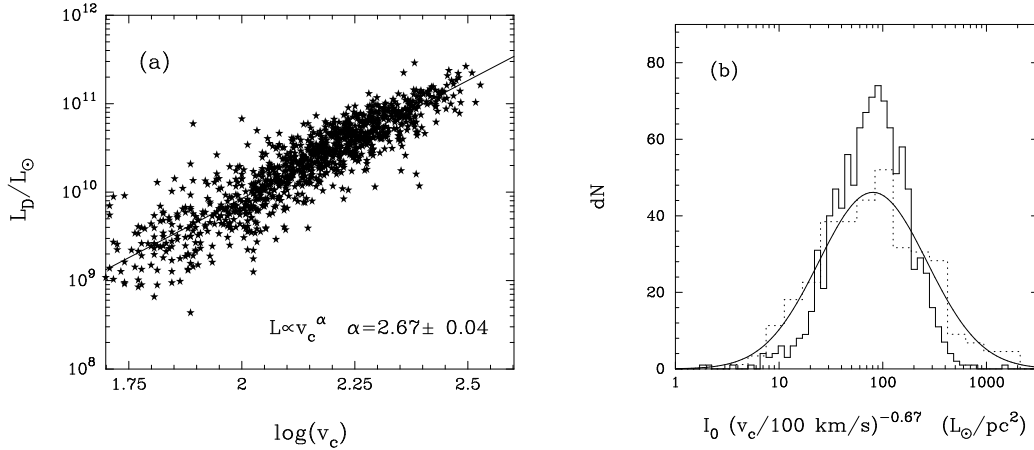


**Figure 2.** (a) shows the disc luminosity of the Byun & Freeman sample plotted against circular speed  $v_c$ . The line shows a least squares power law fit  $L_c \propto v_c^\alpha$  with  $\alpha = 2.67$ . (b) compares the distribution of  $I_0 v_c^{(2-\alpha)}$  for the Byun & Freeman sample (solid histogram) with the distribution of  $1/\lambda^2$  determined for haloes in the CDM simulation, scaled to have approximately the same mean as the observations, (dotted histogram) and the best-fitting lognormal distribution for  $\lambda$  (solid line). If the disc component conserves angular momentum during collapse then  $I_0 v_c^{(2-\alpha)}$  should be distributed as  $1/\lambda^2$ .

gives an exponent  $\alpha = 2.67 \pm 0.04$ . If we equate the specific angular momentum of the disc to  $j(R_H)$  as given by equation 5 at fixed  $v_c$ , then the collapse factor of the disc is related to the spin parameter of the halo according to

$$\alpha R_H = \frac{\sqrt{2}}{\lambda}, \quad (8)$$

(Fall & Efstathiou 1980). If the gas conserves its angular momentum during collapse, then a disc that forms in a halo with a low value of  $\lambda$  will collapse by a large factor so ending up with a high mean surface mass density; likewise a disc that forms in a halo with a high value of  $\lambda$  will end up with a low mean surface mass density. The large scatter in  $\lambda$  from tidal torques should therefore be reflected in the spread of surface mass densities and surface brightnesses of disc systems. The disc luminosity of an exponential disc is related to the central surface brightness,  $I_0$ , according to  $L_D = 2\pi I_0 \alpha^{-2}$ , thus from equations 7 and (8),

$$I_0 v_c^{(2-\alpha)} \propto \frac{1}{\lambda^2}. \quad (9)$$

Fig. 2b shows the distribution of  $I_0 v_c^{-0.67}$  for the Byun-Freeman sample, compared to the distribution of  $1/\lambda^2$  for haloes in the N-body simulations. The mean of the  $1/\lambda^2$  distribution has been adjusted to match the mean of the observational data points. The observed distribution plotted in Fig. 2b peaks at about  $100 L_\odot/\text{pc}^2$  and has a broad distribution comparable to, but not quite as broad as the distribution of  $1/\lambda^2$ . It is easy to think of reasons why the observed distribution might be artificially narrow, for example, the Byun-Freeman sample could be incomplete at low and high surface brightness, and perhaps some objects with large collapse factors produce spheroidal systems. Indeed there is a large literature on observational selection effects and the surface brightness distributions of galaxies (e.g. Disney 1976; Allen & Shu 1979; Phillipps & Disney 1986; Dalcanton, Spergel and Summers 1997). Qualitatively,

however, the above comparisons show that the mean angular momenta of disc systems, and their scatter, fit well with a picture in which disc galaxies form at recent epochs by the collapse of extended gaseous atmospheres within dark haloes. Fig. 2b suggests that disc galaxies form within dark haloes with a wide range of  $\lambda$  values, *i.e.* that the angular momentum of the halo is not a critical factor in determining whether a disc system forms. Within this picture, however, the angular momentum of the disc component must be approximately conserved during collapse.

In the following sections, we will investigate this picture numerically in some detail, showing that cooling and feedback processes are crucial in determining the angular momentum of the disc component, as well as in determining the fraction of the baryonic gas that can cool.

### 3 NUMERICAL TECHNIQUES

Our cosmological simulations were performed using two different self-consistent, 3-dimensional, N-body codes, TREE-SPH (Hernquist & Katz 1989) and GRAPESPH (e.g. Steinmetz 1996). These codes are capable of evolving systems containing both collisionless material (*i.e.* stars and dark matter) and gas.

Smoothed particle hydrodynamics, in which gas is partitioned into fluid elements, is used to model hydrodynamical interactions between gas particles (Lucy 1977, Gingold & Monaghan 1977). The self-gravitating fluid elements are represented as particles that evolve according to Lagrangian hydrodynamic conservation laws which take into account local effects arising from pressure gradients and viscosity. The equation of state is that for an ideal gas,  $P = (\gamma - 1)\rho u$  where  $\gamma = 5/3$ ,  $\rho$  is the gas density, and  $u$  is the specific thermal energy. As shocks can arise in the gas, an artificial viscosity is required to maintain numerical stability. The form of

artificial viscosity used in both codes is similar to that used by Navarro & Steinmetz (1997), *i.e.* modified by the curl of the velocity field to reduce the shear component.

Radiative cooling and star formation are included in the codes. The primordial gas is assumed to have a hydrogen fraction of  $X = 0.76$  and a helium fraction of  $Y = 0.24$  by weight. Cooling is computed using the ionization, recombination, and cooling rates from Black (1981, Table 3) with the modifications suggested by Cen (1992) for temperatures  $T \gtrsim 10^5$ . Radiative cooling does not proceed below a minimum temperature  $T_{min} = 10,000\text{K}$ . The star formation is implemented differently in the two codes and will be described in Sections 3.1 and 3.2.

### 3.1 TREESPH

TREESPH computes gravitational forces between particles using a hierarchical tree algorithm that groups distant particles into nested cells. The potentials of the cells are then approximated with a multipole series truncated at the quadrupole. When computing the force on a particle, TREESPH calculates the ratio of the current cell size to the distance between the cell and the particle. For values  $\leq \theta$ , a specified tolerance parameter, the force from the cell is treated as a whole; otherwise, the next cellular subdivision is considered. A spline kernel is used to soften the gravitational potential in order to reduce two-body relaxation.

In TREESPH, individual smoothing lengths,  $h_i$ , are calculated for each gas particle and updated to ensure that  $N_{smooth} = 25 - 45$  neighbours are contained within a sphere of radius  $2h_i$ . In addition to individual smoothing lengths, individual timesteps are permitted for each particle. The largest time step for these TREESPH simulations is  $\Delta t = 6.24 \times 10^6$  years; the smallest number of timesteps in which a particle can reach  $z = 0$  is  $N_{step} = 2000$ . Smaller timesteps are chosen for particles in dense regions, using the criterion  $a_i v_i \Delta t_i \leq e_{tol} E_i$  where  $a_i$  and  $v_i$  are the acceleration and velocity of the particle, and  $e_{tol} = 0.1$  determines the fractional accuracy of the integrations.  $E_i$  is the maximum of the mean specific kinetic energy and one sixth of the mean specific potential energy of the system (Ewell 1988). Particles in the highest density areas are allowed to reduce their timesteps by up to a factor of eight.

Thermal energy is computed from

$$\frac{du_i}{dt} = \sum_j m_j \left( \frac{P_i}{\rho_i} + \frac{1}{2} \Pi_{ij} \right) \mathbf{v}_{ij} \cdot \frac{1}{2} [\nabla_i W(r_{ij}, h_i) + \nabla_i W(r_{ij}, h_j)] - \frac{\Delta_i}{\rho_i} \quad (10)$$

where the first term is due to adiabatic processes, the second term accounts for the viscosity, and the third term includes the remaining nonadiabatic radiative cooling.  $W$  is the SPH smoothing kernel, which is implemented in the gather-scatter formulation of Hernquist & Katz (1989). A semi-implicit method of integrating the energy equation is employed. An explicit integration using a timestep that is half of the shortest SPH particle timestep is performed on the adiabatic terms whereas an implicit integration is performed on the nonadiabatic thermal heating and cooling processes. In high density regions, the cooling time step can become so short that it is computationally impractical to employ it. Thus, in order to avoid numerical errors in the integration of the thermal energy, the cooling rate is damped

so that a particle can lose no more than half its thermal energy during a cooling time step (Katz & Gunn 1991).

Star formation, in which gas particles which meet the formation criteria are allowed to form a ‘star’ wholly and instantaneously, has been included in TREESPH. The criteria for star formation are similar to those of Katz (1992). First, gas particles in collapsing regions are found, using  $\nabla \cdot \mathbf{v}_i < 0$  as the condition for the existence of a convergent flow. Second, the flow is tested for Jeans instability. The particle is locally Jeans unstable if the sound crossing time is shorter than the dynamical time. Each gas particle in a converging flow with

$$\frac{h_i}{c_i} > \frac{1}{\sqrt{4\pi G \rho_i}}, \quad (11)$$

where  $c_i$  is the local sound speed, is thus a candidate for star formation. However, regions in which the gas density has decreased drastically during previous star formation will not contract as readily as physically expected due to gravitational softening. Because gas particles in these high star formation regions will otherwise be prevented from forming stars through inability to meet the Jeans instability criterion, that criterion is not applied to gas in softened regions with

$$K_s \left( \frac{\pi \epsilon_i}{\sqrt{2}} \right)^2 \frac{\mu m_H G}{k T_i} \rho_i > 10, \quad (12)$$

where  $K_s = 0.89553$  is a constant derived from a calculation of the Jeans mass (Katz 1992),  $\epsilon_i$  is the softening length,  $m_H$  is the mass of a hydrogen atom,  $k$  is the Boltzmann constant, and  $T_i$  and  $\rho_i$  are the gas temperature and density. Third, if the cooling time,  $t_c = u_i (du_i/dt)^{-1}$ , is shorter than the local dynamical time,  $t_d = (4\pi G \rho_i)^{-1/2}$ , then gas pressure will not inhibit the collapse of the gas particle and it may form a star. However, because radiative cooling is cut off at  $T_{min} = 10,000\text{K}$ , gas particles at low temperatures have long cooling times. In order to avoid an artificial cessation of star formation in low temperature regions, gas particles with  $T < 30,000\text{K}$  which otherwise meet the criteria are allowed to form stars with a cooling time set to the dynamical time  $t_c = t_d$ . The local rate of star formation is

$$\frac{d\rho_*}{dt} = \frac{-d\rho_g}{dt} = \frac{c_* \rho_g}{t_c} \quad (13)$$

where  $c_* = 0.1$  is a dimensionless star formation parameter. The probability that a gas particle will form a star in time  $\Delta t$  is

$$p_* = 1 - e^{-c_* \Delta t / t_c}. \quad (14)$$

A random number is generated for each star candidate; if it is less than  $p_*$ , the gas particle loses its SPH characteristics and becomes a collisionless star particle.

For these cosmological simulations, TREESPH evolves the haloes from the initial redshift to  $z = 0$  using physical coordinates with isolated boundary conditions.

### 3.2 GRAPESPH

The version of GRAPESPH we employ has evolved from the TREESPH code of Navarro & White (1993; hereafter NW). Rather than using the mutual nearest-neighbour binary tree (Benz *et al.* 1990) of the original implementation in order to calculate gravitational forces and find neighbours

for the SPH force evaluation, the special-purpose GRAPE-3Af hardware (Sugimoto *et al.* 1990) has been harnessed to perform these tasks. This machine carries out a parallelised direct summation over all particles and very rapidly returns the forces and neighbour lists. All hydrodynamical forces are then calculated on the host workstation. The adaptations which convert a TREESPH code into a GRAPESPH code have been described in detail by Steinmetz (1996).

Both individual timesteps and individual gas particle smoothing lengths were used. As the GRAPE only returns ‘gather’ neighbours, that is those within distance  $h_i$  of gas particle  $i$ , the neighbour search radius is taken to be  $\sqrt{1.5}$  times the smoothing length. This should ensure that the actual number of mutual neighbours, which satisfy  $h_i + h_j < 2$  times the particle separation, lies within the range 25 – 45.

The gravitational forces are calculated assuming a Plummer softening law. For each particle, the total acceleration due to gravity is found in two steps. First, the acceleration arising from all gas particles is found, and then that resulting from dark matter and stars is incremented. A different gravitational softening parameter is used in these two separate force evaluations.

A simplified version of the star formation algorithm described by NW was adopted. Any gas particle in a sufficiently high density, collapsing region is considered to be a potential star-forming particle. These two constraints can be expressed as

$$\rho_i > \rho_{\text{crit}*} = 7 \times 10^{-23} \text{ kg m}^{-3} \quad (15)$$

and

$$\nabla \cdot \mathbf{v}_i < 0. \quad (16)$$

The local dynamical time is then defined by

$$\tau_{\text{dyn}} = \sqrt{\frac{3\pi}{16G\rho_i}}. \quad (17)$$

If conditions (15) and (16) remain satisfied for the ensuing dynamical time then the gas particle converts entirely to a star particle. Should either of these constraints be violated during this probationary period then the gas particle is no longer considered to be star-forming and it remains gaseous.

### 3.3 Contrasting the Codes

The softening of the gravitational interaction between two particles differs in the two codes. In GRAPESPH, the potential is of the form corresponding to a Plummer density profile,  $\Phi \propto (r^2 + \epsilon^2)^{-1/2}$ . However, the acceleration calculated using a Plummer model softening converges to the Kepler value relatively slowly. In codes like TREESPH, in which distant particles are assigned to cells and their potentials are represented by quadrupole expansions, the cells are assumed to be point-like rather than extended. Thus, a softening in which the acceleration quickly converges to the Kepler form is advantageous. In TREESPH, the gravitational potential is softened using the spherically symmetric spline kernel suggested by Monaghan & Lattanzio (1985) because it has compact support and is identical to the Kepler form for  $r \geq 2\epsilon$ . For the effective softening to be similar in both codes, the TREESPH softening lengths must have values approximately twice those of the GRAPESPH softening lengths.

The star formation algorithms employed within the two codes derive from Katz (1992) and NW. They are similar in requiring that a gas particle be able to form a star only if it is in a converging flow. However, other criteria differ. This version of GRAPESPH, unlike TREESPH and NW, does not use the Jeans instability criterion for creating star particles nor does it define a star formation rate. Like NW, GRAPESPH defines a critical density, above which the cooling time is less than the dynamical time. The two GRAPESPH criteria are applied to each particle when it is advanced. The criteria are monitored over the dynamical time for each ‘successful’ gas particle after which, if they are not violated, a star is formed. In general, the delay is  $\lesssim 10^7$  years. In TREESPH, the criteria are checked at each system timestep of  $\Delta t = 6.24 \times 10^6$  years; a random number of gas particles which meet the star-forming criteria are chosen to form stars immediately. The effect of these differences is that the GRAPESPH simulations produce more stars between  $z = 1$  and 0.8 while, afterwards, the star formation rate in the TREESPH simulations is higher. By  $z = 0$ , the number of GRAPESPH stars is some 75–90% of the number of TREESPH stars. This difference is due to the additional TREESPH formation criteria which allow stars to continue to form in regions of high star formation where the gas density has decreased due to the transformation of gas particles to stellar particles. Qualitatively, the GRAPESPH criteria act to mimic larger supernova feedback effects in regions of high star formation.

## 4 INITIAL CONDITIONS

The initial conditions for our simulations are generated using a nested hierarchy algorithm similar to that described by Katz & White (1993). The idea is to select haloes from the dissipationless CDM simulation described in Section 2, and then to re-simulate them at higher mass resolution using the SPH codes of the previous section. This technique has been used by Navarro, Frenk & White (1995b) and Eke, Navarro & Frenk (1998), in SPH simulations of clusters of galaxies and by Navarro & Benz (1991), Quinn, Katz & Efsthathiou (1996), Navarro & Steinmetz (1997) and others in SPH simulations of galaxy formation.

### 4.1 Selection of the Haloes

Haloes with a density contrast  $\Delta \approx 200$  were located at  $z = 0$  in the N-body simulation using the group finding algorithm described in Section 2. The haloes were ordered by circular speed. We then visually examined plots of the halo particles at various output times and selected five examples for simulation with the SPH codes. The haloes were chosen to have a range of circular speeds between 300  $\text{kms}^{-1}$  and 150  $\text{kms}^{-1}$ , to be far from much more massive haloes, and not to have merged with a comparable mass system since  $z = 1$ . Parameters for the 5 chosen haloes are given in Table 1. The first condition selects objects with circular speeds in the range observed for normal luminous disc systems. The second criterion eliminates satellite systems near the outer parts of massive systems, for which our tree codes and hierarchical initial conditions algorithm are ill-suited. The third criterion eliminates haloes that undergo major merger

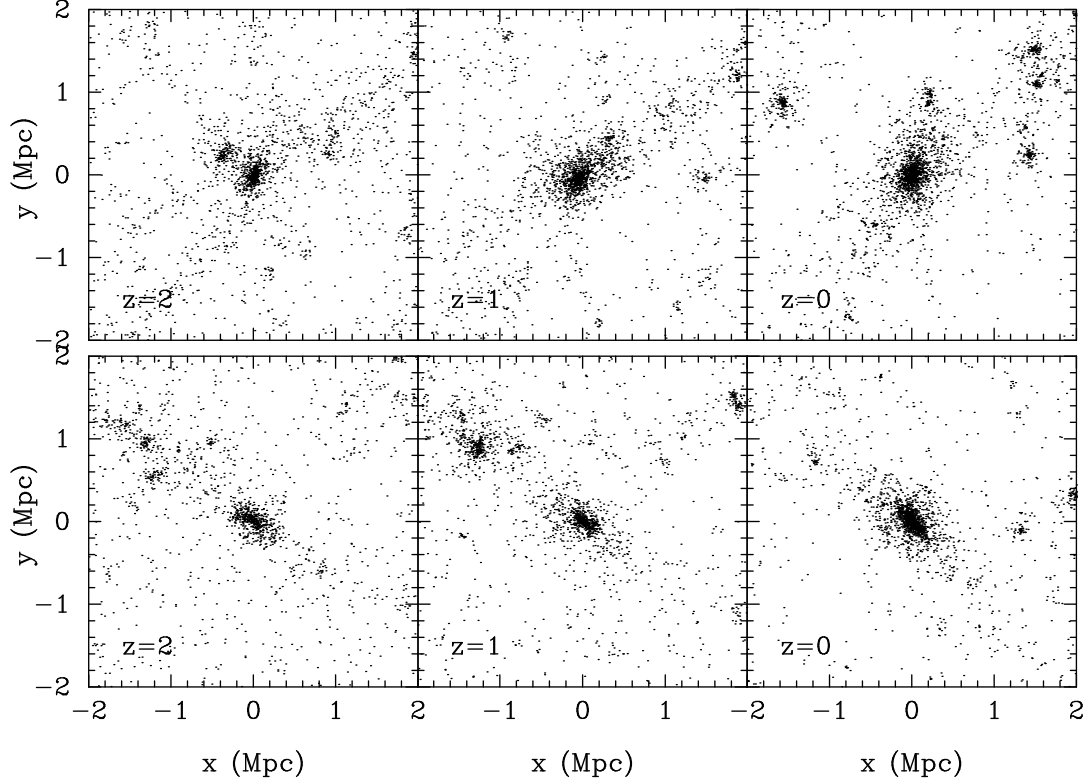


**Figure 3.** The evolution of two haloes from the dissipationless N-body simulation described in Section 2. x-y projections are shown of the particles located within a box of comoving length 4 Mpc centred on the dominant subclump at  $z = 2$ ,  $z = 1$  and  $z = 0$ . The upper panel shows the evolution of Halo 2 listed in Table 1, with a final circular speed of  $v_c = 249 \text{ km s}^{-1}$ . The lower panel shows the evolution of a halo with a nearly identical final circular speed,  $v_c = 247 \text{ km s}^{-1}$ , that we did not simulate with the SPH codes because it evolves by the merger of two comparable mass components at  $z < 1$ .

events at low redshifts and so preferentially selects regular objects that grow by the accretion of smaller systems at low redshifts. Nevertheless, even with this selection criterion, the typical halo mass within an overdensity of  $\Delta = 200$  nearly doubles between a redshift of 1 and 0 (see Table 1).

**Table 1: Parameters for the five haloes chosen for SPH simulation**

Halo	$v_c$ (km/s)	$M_H \times 10^{11} M_\odot$		$\lambda_H$	$L_{hr}$ (Mpc)
		$z = 0$	$z = 1$		
1	265	70.5	35.2	0.050	6.00
2	249	57.7	38.8	0.020	6.08
3	176	25.1	14.2	0.031	4.92
4	160	21.5	11.8	0.040	5.64
5	157	20.1	16.7	0.032	4.84

*Notes to Table 1:* The first column gives the halo number, used throughout this paper. The second column gives the circular speed computed from equation 1. The third column gives the mass of the halo at  $z = 0$ , and the fourth column gives the mass of the dominant subclump at  $z = 1$  identified by running the group finding algorithm with a link parameter  $b = 0.2$ . The fifth column gives the  $\lambda$  parameter of the halo at  $z = 0$ . The final column gives the comoving size of

the box used to generate high resolution initial conditions as described in Section 4.2.

The upper panel in Fig. 3 shows an x-y projection of Halo 2 at  $z = 2$ ,  $z = 1$  and  $z = 0$ . The lower panel shows the evolution of a halo with almost identical circular speed that we decided not to simulate because it evolves by the merger of two comparable mass subunits at  $z < 1$ . The selection criteria that we have imposed will bias statistics of the frequency of disc galaxy formation in CDM models, and this must be borne in mind when interpreting some of the results presented in the next two Sections. In particular, the last column of Table 1 shows that our selection criteria bias against haloes with high values of  $\lambda$ . This is because haloes with high  $\lambda$  often contain two distinct subclumps, or are near much more massive systems.

## 4.2 Generation of High Resolution Initial Conditions

The particles within a sphere of radius 400 kpc around the centre of mass of the halo at  $z = 0$  were traced back to the initial conditions. The smallest cubical box containing all of these particles was located, defining the region to be resampled at higher mass resolution. The comoving box sizes of the high resolution regions for each halo are listed in the final column of Table 1; typically a box of comoving size

5–6 Mpc is required. Having located the size and location of the high resolution region, initial conditions for the SPH simulations were generated as follows.

[1] Distribute  $N_{hr}^3$  particles on a regular lattice within the high resolution box of size  $L_{hr}$ .

[2] Generate displacements of these particle positions using the algorithm of Efstathiou *et al.* (1985) with the identical amplitudes and phases used to generate the initial conditions of the low resolution simulation, but with the initial power spectrum sharply truncated at the Nyquist frequency of the low resolution particle grid  $k_n = \pi N_p / L_{box}$ .

[3] Generate additional displacements to add in the missing small-scale power between the Nyquist frequencies of the low resolution particle grid and the high resolution particle grid  $k_{n'} = \pi N_{hr} / L_{hr}$  from the appropriate CDM power spectrum.

[4] Add  $M$  nested layers of massive particles to represent the tidal field of the surrounding matter. The particles in these outer layers are arranged on lattices such that the lattice spacing increases by factors of two outwards from the high resolution region and particle masses increase by factors of eight, as described by Katz & White (1993, see their Fig. 1). Five layers were chosen to match exactly the total mass,  $M_{box}$ , contained in the low resolution N-body simulation.

[5] Generate displacements for these outer particles as in [2] above, but with the power spectrum sharply truncated below the Nyquist frequency of each layer. This last step prevents aliasing of small-scale power from affecting the representation of the tidal field.

For the simulations described in the next section, we used a high resolution region represented by  $27^3$  particles. The outermost of the five low resolution layers of dark matter particles was stripped off each halo, because tests revealed that it had a negligible effect on the evolution of the particles within the high resolution region. The total mass,  $M_{tot}$ , of the four remaining layers and the interior high resolution particles was calculated and the new outermost layer was truncated by removing all particles within radius

$$r = \frac{1}{2} \left( \frac{M_{tot}}{M_{box}} \right)^{1/3} L_{box}, \quad (18)$$

from the centre of the simulation. This produces a spherical distribution of the outermost high mass particles. Each dark matter particle in the high resolution layer was reduced in mass by 10% and overlaid with a gas particle of mass  $m_{gas} = 0.1 m_{dark}$  to produce a high resolution region containing gas. The masses of dark matter and gas particles in the simulations range from  $3.6 - 7.1 \times 10^8 M_\odot$  and  $4.0 - 7.9 \times 10^7 M_\odot$ , respectively.

The total number of particles is  $N_{tot} = 41136$ , with the low resolution layers having  $N_1 = 1178$ ,  $N_2 = 386$ ,  $N_3 = 152$ , and  $N_4 = 54$ . In the TREESPH simulations, the gas particles were offset in position from the dark matter particles by a fraction of a softening length to avoid numerical difficulties in constructing a tree containing all particles.

## 5 NUMERICAL SIMULATIONS

### 5.1 Parameters of The Simulations

Each of the five haloes of Table 1 was simulated at high mass resolution with TREESPH and GRAPESPH. As we

will show in subsequent sections, the softening of the gravitational force law has a large effect on the calculations. In the TREESPH simulations, the high resolution dark matter particles are assigned gravitational softening lengths of  $\epsilon_{dark} = 10.4$  kpc. The gas and star particles in TREESPH have  $\epsilon_{gas} = \epsilon_{stars} = 2.6$  kpc to allow better resolution of the overdense regions in which the galaxies form. Larger softening lengths are adopted for the low resolution layers of high mass particles according to  $\epsilon_{layer} = (m_{layer}/m_{dark})^{1/3} \epsilon_{dark}$ . In the GRAPESPH simulations, the gravitational forces are computed assuming a Plummer force-law with softening lengths of  $\epsilon_{dark,star} = 5$  kpc for the dark matter and star particles and  $\epsilon_{gas} = 1$  kpc. With these choices, the softened force laws for the gas and high resolution dark matter particles are similar in the two codes. However, the softening adopted for the stars in GRAPESPH is about twice as large as the softening adopted for the star particles in TREESPH. This is because in the GRAPESPH code, gravitational forces for all collisionless particles (dark matter and stars) are computed in one single parallelized direct summation and thus have the same softening.

Both codes employ variable timesteps. Particles in the TREESPH runs completed the evolution from the initial redshift of  $z = 7.4$  to  $z = 0$  in 2000 to 16000 timesteps and a typical simulation with 41136 particles required approximately 100 hours to run on an DEC Alpha 4100 5/300. Evolution of the particles in the GRAPESPH simulations required typically  $\sim 100 - 40000$  steps and  $\approx 45 - 65$  CPU hours to run to completion from  $z = 7.4$  to  $z = 0$  on the GRAPE machine at Edinburgh.

In most previous simulations of this type, the gas has been allowed to cool radiatively with no other energy input except that provided by gravitational shock-heating and, in some simulations, a uniform photoionizing background radiation (see *e.g.* Quinn *et al.* 1996; Navarro & Steinmetz 1997). In some simulations, attempts have been made to mimic energy injection into the intergalactic medium by supernovae (Katz 1992; NW). Broadly speaking, these have involved either injecting energy directly as heat into the gas, or into bulk motion so reversing the flow of gas into high density regions. As discussed by NW, neither approach is satisfactory. Energy supplied as heat into high density gas is radiated away so efficiently that it has very little feedback effect. On the other hand, it is easy to reverse the flow of gas by injecting energy into bulk motions, but the feedback effects are then extremely sensitive to the specific algorithm and parameters that are used. We believe that a more realistic description of feedback requires the ability to model a multiphase gas component, in which cool high density gas can coexist spatially with an outflowing hot lower density gas component. Modeling such a multi-phase gas medium would require fundamental modifications to the SPH codes described here, and so is well beyond the scope of this paper. Some provisional attempts along these lines, using a Eulerian gas dynamic code, are described by Yepes *et al.* (1997).

Nevertheless, as described in the Introduction, our thesis in this paper is that feedback processes are critical in determining the angular momenta of disc systems. The key process that we wish to model is the late infall of gas into a dark matter halo. The numerical simulations of Navarro & Steinmetz (1997) described in the introduction show that, in



the absence of any feedback, gas collapses at high redshifts into dark matter subclumps that later merge, losing most of their orbital and internal angular momentum to outer halo particles. If, however, feedback processes can prevent some significant fraction of the gas from collapsing at high redshifts, then there is a possibility that this residual gas can collapse within a more uniform and slowly evolving halo to form a disc system whilst conserving its angular momentum. Such a formation scheme for disc systems seems essential in hierarchical clustering theories, since the discussion of Section 2 shows that the angular momenta of disc systems can only be understood if the gas approximately conserves its angular momentum during collapse.

In this paper, we have chosen a particularly simple scheme to model feedback processes. We evolve the gas component adiabatically until a specified redshift  $z_{\text{cool}}$ , at which point we switch on radiative cooling with a cooling rate  $\Lambda$  as described in Section 3. For most of the runs, we adopted  $z_{\text{cool}} = 1$ . Some runs were done with  $z_{\text{cool}} = 4$  and  $z_{\text{cool}} = 0.6$  to illustrate the sensitivity of angular momentum evolution to the epoch of gas collapse. Two simulations were done in which the cooling rate  $\Lambda$  was suppressed by a factor,

$$g(z) = (1+z)^\alpha \exp\left(-\left(z/z_c\right)^2\right), \quad \alpha = -1.5, \quad (19)$$

where  $z_c$  is a parameter. The parameter  $\alpha$  was fixed to  $\alpha = -1.5$  by an analytical calculation of cooling within an isothermal halo so that discs would grow roughly linearly with time. Simulations were done with  $z_c = 1$ , almost completely eliminating high redshift cooling, and with  $z_c = 4$ . Table 2 gives a complete list of the SPH simulations that were run for this paper.

## 5.2 Comparison of Codes

The simulations described here are at the limit of what is possible with present-day computers, thus it is important to understand the limitations imposed by the computational scheme, such as limited mass resolution, gravitational softening *etc.* In this subsection, we thus describe in some detail the differences in the evolution of two haloes (2 and 3) run with the two codes.

### 5.2.1 Morphologies

Fig. 4 shows projections of the dark matter and gas distributions at  $z = 1$  evolved with cooling suppressed (Runs 4, 5, 11, and 12). The left-hand panels show the particle distributions evolved with TREESPH and the right-hand panels those evolved with GRAPESPH. Although the two codes produce dark matter and gas distributions that are closely similar, we were surprised to see some differences. Perhaps the most striking variations can be seen in the relative positions and morphologies of the four dark matter concentrations to the left of Halo 3. The structure of the central halo itself also appears to be slightly different in the two runs.

To explore these morphological differences, and determine whether they were caused by differences in the treatment of the gas component, we re-evolved Halo 3 with the two codes from  $z = 7.4$  to  $z = 1$  using only dark matter particles. First, the haloes were run with the same computational parameters as Runs 11 and 12. Projections at  $z = 1$

**Table 2: List of Simulations**

Run	Halo	Code	$z_{\text{cool}}$	$z_c$
1	1	TREESPH	1	–
2	1	GRAPESPH	1	–
3	1	TREESPH	4	–
4	2	TREESPH	1	–
5	2	GRAPESPH	1	–
6	2	TREESPH	4	–
7	2	GRAPESPH	4	–
8	2	GRAPESPH	0.6	–
9	2	TREESPH	–	1
10	2	TREESPH	–	4
11	3	TREESPH	1	–
12	3	GRAPESPH	1	–
13	4	TREESPH	1	–
14	4	GRAPESPH	1	–
15	5	TREESPH	1	–
16	5	GRAPESPH	1	–
17	5	TREESPH	4	–
18	5	TREESPH	0.6	–

*Notes to Table 2:* The first column lists the run number, the second gives the halo number as in Table 1 and the third column lists code used to run the simulation. The fourth column lists the redshift  $z_{\text{cool}}$  at which radiative cooling was switched on. Where this is blank, we suppressed the cooling rates by the factor given in equation 19 with parameter  $z_c$  listed in the fifth column.

are shown in panels (a) and (b) of Fig. 5, which can be compared directly with the dark matter plots shown in Fig. 4. The differences between the particle positions computed from the two codes are almost identical to those seen in Fig. 4, implying that they do not arise merely from differences in the treatment of gas. Rather, the differences must arise from errors in the gravitational forces or the time-integration of the equations of motion. We therefore reran these dark matter only runs using different code parameters. For TREESPH, we improved the accuracy of the forces by changing the force-tolerance parameter from the default value  $\theta = 0.8$  to  $\theta = 0.5$ . In GRAPESPH, the force calculation is hardwired into the GRAPE with, typically, a  $\sim 2\%$  dispersion in the forces between particle pairs (see Okumura *et al.* 1993). Since the force accuracy cannot be adjusted in the GRAPESPH code, we reran the simulation employing three times as many timesteps. Snapshots from these two runs are shown in panels (c) and (d) of Fig. 5, and show clearly that force errors in TREESPH are the main cause of the discrepancies. For many purposes these small errors are unimportant, but they can lead to different merger histories and to differences in the radial profiles of some quantities sensitive to the presence of substructure, *e.g.* plots of the specific angular momentum with radius (see Figures 8 and 12 below).

The stellar condensations that form in Runs 4 and 5 (Halo 2) and Runs 11 and 12 (Halo 3) are shown in Fig. 6. These ‘galaxies’ have been rotated so that each panel shows a projection along two of the principal axes; the TREESPH  $X - Y$  and  $X - Z$  projections are shown on the left, and the corresponding GRAPESPH  $X - Y$  and  $X - Z$  projections

**Figure 4.** Projections of the dark matter and gas components at  $z = 1$  for two haloes (Runs 4, 5, 11, and 12) evolved with the TREESPH and GRAPESPH codes.

are shown on the right. Halo 2 evidently forms a disc system in both simulations. Similar numbers of stars are formed with the two codes, but there are noticeable differences attributable mainly to the much larger stellar softening length used in GRAPESPH. The TREESPH galaxy is clearly more concentrated, and has a much thinner disc.

Much larger differences are evident in the evolution of the Halo 3 stellar systems, shown in the lower panels of Fig. 6. The TREESPH galaxy shows disc-like structure at both redshifts. At  $z \approx 0.5$ , the main component in the GRAPESPH simulation is also disc-like, but there is a satellite system containing about 25% of the mass of the main galaxy which is not apparent in the TREESPH panel. The satellite system is present in the TREESPH simulation, but

**Figure 5.** Four simulations of Halo 3, using dark matter only, plotted at  $z = 1$ . Panels (a) and (b) show TREESPH and GRAPESPH using the default computational parameters. These plots are almost identical to the dark matter distributions plotted in Fig. 4 and show distinct differences between the two codes, for example, in the location of the four clumps to the left of the main central mass concentration. Panels (c) and (d) show a TREESPH simulation employing a more accurate force computation, and a GRAPESPH simulation using smaller timesteps. Panels (c) and (d) are almost identical, and similar to the default GRAPESPH simulation, showing that force errors in TREESPH cause most of the discrepancies.

the slight difference in output redshifts (0.49 as opposed to 0.46 for GRAPESPH) coupled with the high relative speed of the intruder conspire to move it outside the region plotted in the figure. In both runs the incoming satellite makes a first fly-by of the main disc at  $z \sim 0.4$ , with the eventual merger occurring at  $z \sim 0.15$ . However, because of the more extended structure of the GRAPESPH central stellar disc that results from the larger softening, the interaction and subsequent accretion of the satellite system is more disruptive in this case. As a consequence the merger event has a preferentially destructive effect on the GRAPESPH disc, leaving a spheroidal stellar object at  $z = 0$ , whereas the TREESPH disc survives largely intact. Referring back to Fig. 4, it is the subclump directly below the central clump that is responsible for this collision (the systems to the left do not fall into the centre before  $z = 0$ ). This example shows the sensitivity of the final remnant morphologies to the stellar softening.

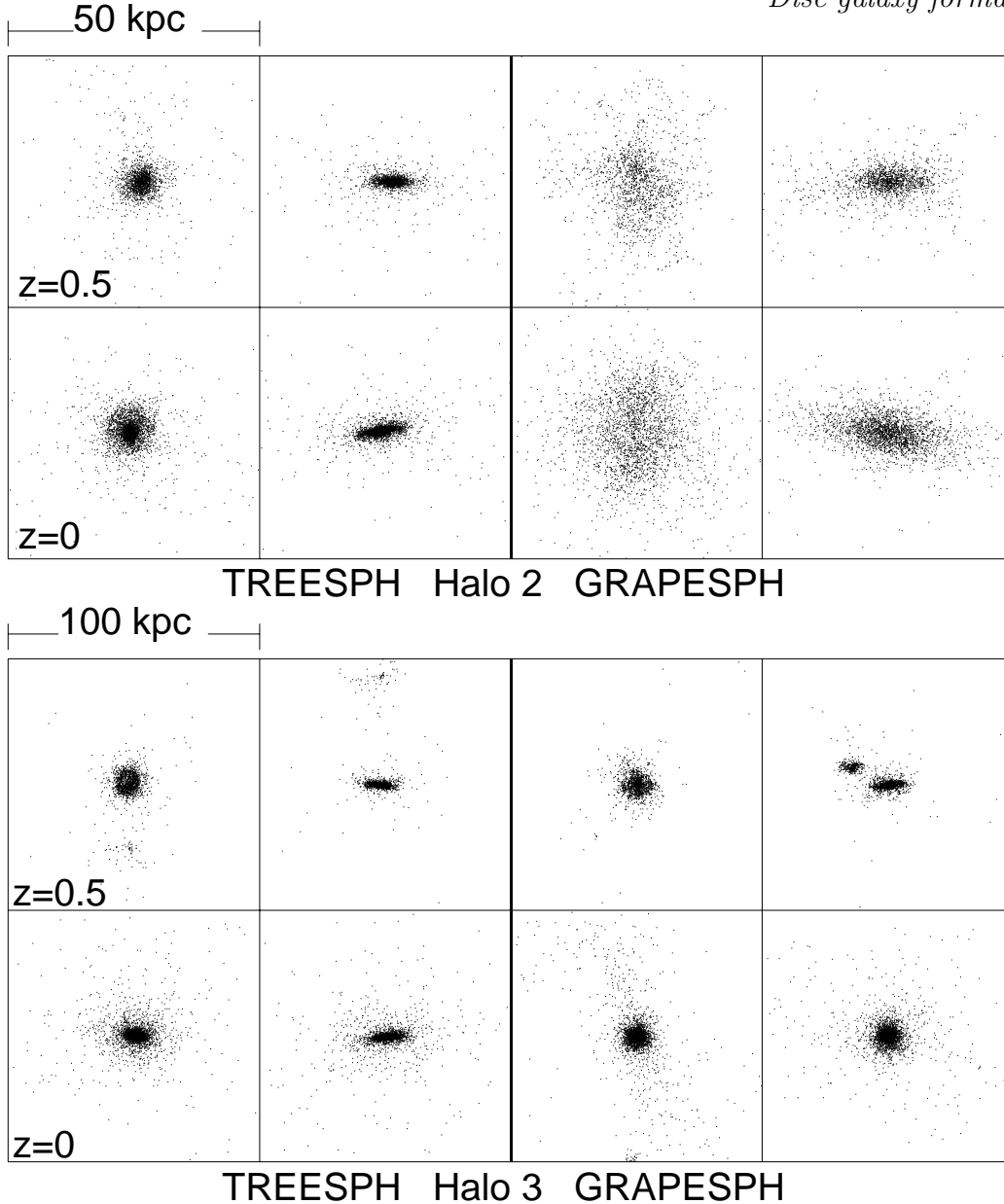


**Figure 6.** Stars in the Halo 2 (Runs 4 and 5) and Halo 3 (Runs 11 and 12) simulations at  $z \approx 0.5$  and  $z = 0$ . Lefthand panels show the TREESPH simulations projected along the principal axes  $X - Y$  and  $X - Z$  and the righthand panels show the GRAPESPH simulations in the same projections.

### 5.2.2 Star Formation

We define a ‘virial’ radius,  $R_{vir}(z)$ , for each halo by placing a sphere at the centre of mass within which the overdensity is equal to  $\Delta = 178$ . The number of star particles in our simulations within the virial radius at  $z = 0$  lies within the range  $N_{star} = 1700 - 4000$ . In Fig. 7, the stellar mass within a virial radius for the Halo 2 and 3 galaxies is shown over the redshift range  $z = 1$  to  $z = 0$ . The two codes produce a comparable number of stars before  $z = 0.8$ , after which the TREESPH haloes accumulate stellar mass more rapidly. In both codes, stars are accumulated at a faster rate in Halo 2 than in Halo 3. The Halo 2 galaxy has a final stellar mass of  $2.4 \times 10^{11} M_{\odot}$  in GRAPESPH and  $2.7 \times 10^{11} M_{\odot}$  in TREESPH. For Halo 3, the final stellar mass is

$1.17 \times 10^{11} M_{\odot}$  in the GRAPESPH run and  $1.45 \times 10^{11} M_{\odot}$  in the TREESPH run. Halo 2 forms the more massive stellar disc, by about a factor of two.

It is interesting to compare these numbers with the stellar masses of  $L^*$  galaxies. The luminosity function of Efstathiou, Ellis and Peterson (1988) gives  $L_B^* = 5.1 \times 10^{10} L_{\odot}$  for  $h = 0.5$ . Assuming that the mass-to-light ratio of typical discs is  $(M/L)_B \sim 3h$  in solar units, the stellar mass of a typical  $L^*$  disc system is about  $M_{disc}^* \sim 8 \times 10^{10} M_{\odot}$ , *i.e.* somewhat smaller than the masses of the stellar discs that form in Halos 2 and 3. The agreement is close enough, however, that it suggests that the basic physical picture of late infalling gas may account for the masses of disc systems and the origin of the Tully-Fisher relation (equation 7).

Fig. 7 also shows the stellar mass within a virial radius

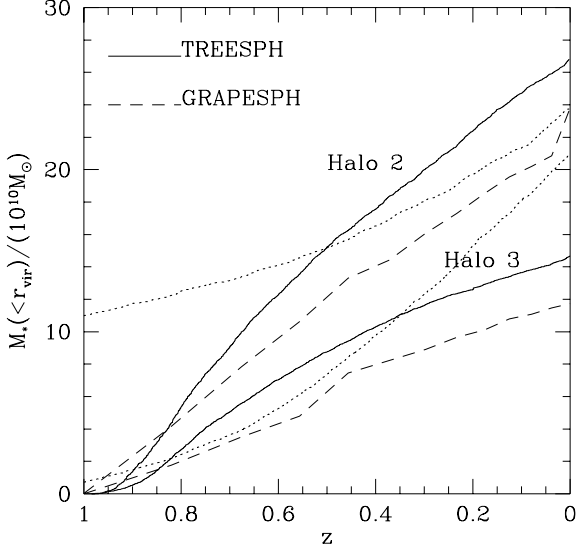


**Figure 7.** Stellar mass within a virial radius for the Halo 2 and 3 galaxies between redshifts  $z = 1$  and  $z = 0$ . Dotted lines are for TREESPH simulations of Halo 2 using the cooling suppression formula,  $g(z)$  with  $z_c = 1$  (bottom line) and with  $z_c = 4$  (top line).

for the two TREESPH simulations of Halo 2 using the cooling suppression formula,  $g(z)$  of equation (19). The bottom dotted line is for a cut-off redshift of  $z_c = 1$  and the top dotted line is for  $z_c = 4$ . In both these simulations, radiative cooling and star formation are turned on at  $z = 4$ . However, star formation is clearly nearly suppressed in the  $z_c = 1$  model until  $z = 1$ , after which stars continue to form slowly until  $z = 0$ . In the  $z_c = 4$  model, nearly half the final total mass of stars has formed by  $z = 1$ , but by  $z = 0$  the galaxy consists of slightly fewer stars than in the simulation with cooling suppressed until  $z_{\text{cool}} = 1$ .

### 5.2.3 Angular Momentum Profiles

The cumulative specific angular momentum profiles of the stellar components in Haloes 2 and 3 are shown in Fig. 8. The total  $J/M$  within a sphere is calculated for 90 equally-spaced radii. The specific angular momenta measured in the TREESPH simulations are about 50% higher than in the GRAPESPH simulations. A small companion at a distance  $r \approx 170$  kpc appears as a stepwise increase in specific angular momentum of Halo 3 in the TREESPH run; this difference to the GRAPESPH run is a consequence of the small differences in the dark matter evolution discussed in Section 5.2.1. In Section 5.3, we will show that angular momentum evolution of the stellar and gaseous components can vary by an order of magnitude or more, depending on what assumptions are made about the physical parameters of the gas (*e.g.* suppression of cooling). These differences in  $J/M$  arising from the input physics are therefore much greater than the differences between the codes seen in Fig. 8.

The most obvious differences in Fig. 8 are in the specific angular momenta in the central regions,  $r \lesssim 20$  kpc. On

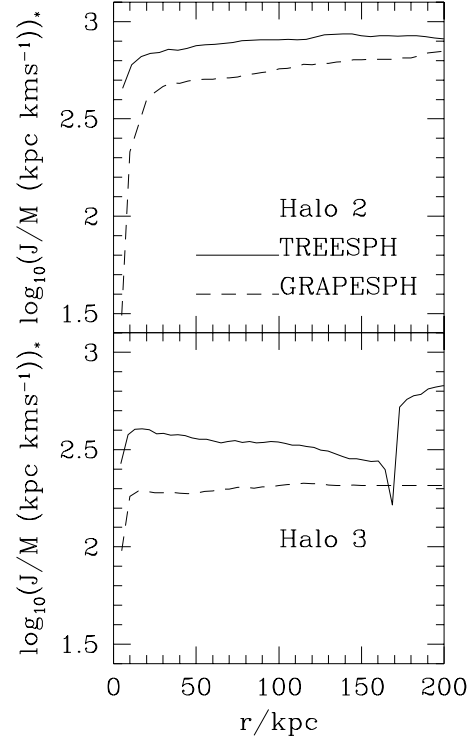


**Figure 8.** Cumulative specific angular momentum profile of the stellar component out to 200 kpc for the Halo 2 and Halo 3 galaxies at  $z = 0$ .

these small scales, the  $J/M$  profile for the GRAPESPH runs declines much more steeply than in the TREESPH runs. Evidently, the angular momentum profiles decline rapidly on scales smaller than a few softening lengths, and this effect is much more pronounced in GRAPESPH because of the much larger stellar softening length. As described in Section 5.2.1, the large softening length of GRAPESPH leads to more diffuse stellar systems, and clearly one cannot expect these simulations to describe accurately the mass and velocity profiles of real disc systems. However, global properties, such as the total stellar mass and angular momentum are much less sensitive to softening.

### 5.2.4 Rotation velocities and velocity dispersions

Fig. 9 shows the projected velocity profiles out to 19 kpc of the Halo 2 and 3 galaxies. The projected velocities are calculated by distributing the particles onto a Cartesian grid in which  $X$ ,  $Y$ , and  $Z$  are chosen to be along the major, intermediate, and minor principal axes, respectively. Each grid cell has dimensions of  $\Delta l = 2$  kpc. A slit with a width of two cells was laid parallel to the axis; results are averaged over the two cells. In Fig. 9, the mean rotation speed of the stars (solid lines) and the projected velocity dispersion (dashed lines) are plotted against major axis distance  $X$ , *i.e.* as would be measured for an edge-on galaxy.

Clear evidence for systematic rotation is seen in both TREESPH runs. In the GRAPESPH runs, the Halo 2 galaxy is rotating with a peak amplitude of about  $80 \text{ km s}^{-1}$ . The difference with TREESPH is, again, primarily a consequence

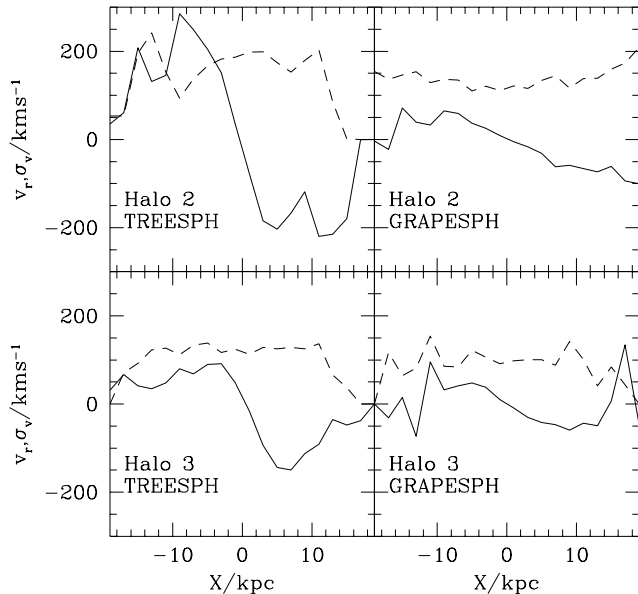


**Figure 9.** Projected major-axis velocity profiles out to 19 kpc for the Halo 2 and 3 stellar systems at  $z = 0$ . Solid lines show the rotation velocity,  $v_r$ ; dashed lines show the projected velocity dispersion,  $\sigma$ .

of the larger GRAPESPH softening length, which inhibits the formation of a compact, rapidly rotating stellar system. Little rotation is seen in the GRAPESPH Halo 3 stars, as might be expected from the lack of any disc in Fig. 6. In comparison, the TREESPH Halo 3 disc rotates with a maximum rotation speed of  $v_r \approx 100$  km/s at  $X \approx 3$  kpc. In both codes, the projected velocity dispersions lie in the range  $\sigma \approx 100 - 200$  km/s, and are roughly constant with radius. The velocity dispersions are comparable to the mean rotation speed in the TREESPH code; thus, neither code succeeds in producing a cool, centrifugally supported, stellar disc. This is almost certainly caused by two-body heating (see *e.g.* Steinmetz & White 1997) which, for discs composed of a few thousand particles, can heat a cold disc to to  $v_r/\sigma \sim 1$  within a few rotation periods. This is consistent with the time-evolution of  $\sigma$  which increases by a factor of  $\approx 2$  between redshift  $z = 1$  and 0.

### 5.2.5 Stellar Mass Profiles

Fig. 10 shows the cumulative stellar mass profile for the Halo 2 and 3 galaxies out to a radius of 25 kpc. This gives an idea of the concentration of the final stellar remnants and of the large differences caused by the softening in GRAPESPH. Even in the TREESPH code, the half-mass radii of the stellar systems are  $\sim 3$  kpc, about equal to stellar softening. This shows that it is possible to form rapidly rotating discs with similar scale lengths to real disc galaxies, though higher resolution calculations are required to model their mass and velocity profiles.

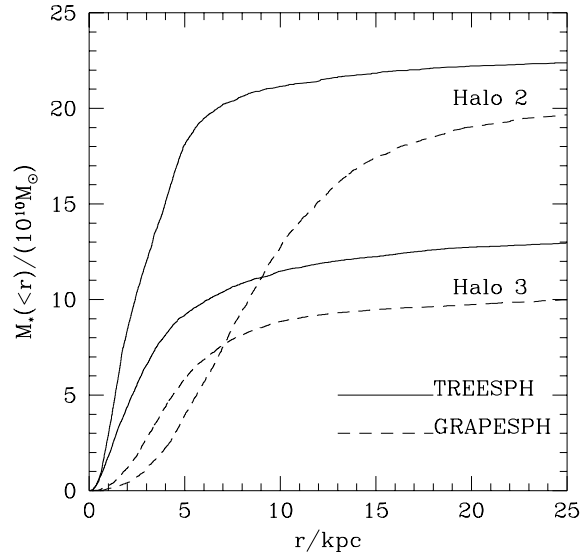


**Figure 10.** Cumulative stellar mass profile of the Halo 2 and 3 galaxies out to a radius of 25 kpc.

### 5.2.6 Summary

The simulation of disc galaxy formation, including star formation, is a complex problem and it is often difficult to assess the accuracy of any particular computational technique. The purpose of this subsection has been to compare the results of evolving identical conditions with two independent SPH codes with the aim of finding which properties, if any, are sensitive to numerical methods. To summarise the findings, the dark matter and gas evolution is broadly similar. However, in one of the 5 haloes (Halo 3), the small differences that do exist produce a significantly different stellar remnant. The overall morphologies of the stellar systems that form in the other four haloes are more similar. Although the star formation algorithms are different in the two codes, they give similar star formation rates and final stellar masses. This is not too surprising because the algorithms are designed to convert high density cool gas into stars on a timescale of order the dynamical time, which is much shorter than the Hubble time when most of the stars form in these simulations. The star formation rate is therefore governed mainly by the rate at which gas infalls towards the halo centres, and this is modeled in a similar way in both codes.

The main differences between the codes are attributable to the larger stellar softening employed in the GRAPESPH simulations. This results in stellar systems that are more extended and have lower rotation velocities than those that form in the TREESPH simulations. Even with TREESPH, the stellar softening of 2.6 kpc is barely adequate to resolve the internal structure of the discs that form. Despite these differences, the global properties of the stellar remnants, *e.g.* their masses and angular momenta, are in reasonably good agreement. In the next Section we will investigate, using both codes, how these global properties depend on the input physics.

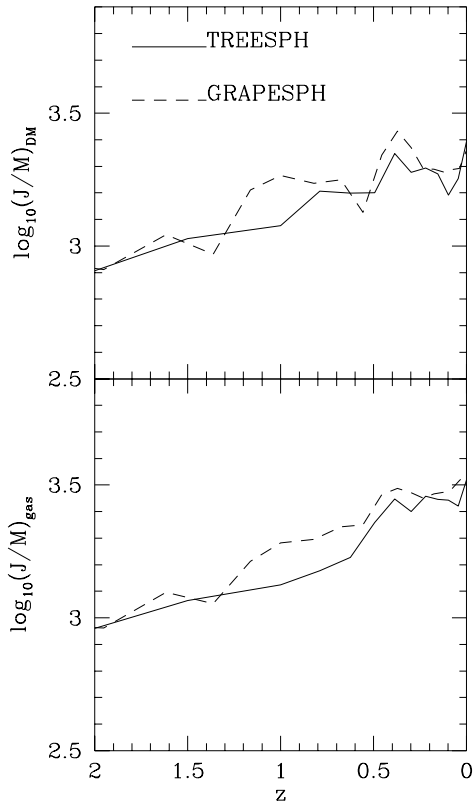


**Figure 11.** Evolution of the mean specific angular momentum within a virial radius of the dark matter (top) and gas (bottom) of the five simulations run with  $z_{\text{cool}} = 1$ . Here and in all succeeding figures,  $J/M$  is in  $\text{kpc km s}^{-1}$ .

### 5.3 Angular Momentum Evolution

We first discuss the evolution of angular momentum in the simulations in which cooling is suppressed until  $z_{\text{cool}} = 1$ . We then discuss how varying  $z_{\text{cool}}$  alters the conclusions.

The accumulation of angular momentum by dark matter haloes and their associated gas proceeds smoothly during the expansion phase before turnaround, growing roughly as  $t^{5/3}$  (White 1984, Barnes and Efstathiou 1987). After collapse, halo angular momentum growth slows and then evolves by abrupt jumps caused by discrete merger events. Since the haloes are all of a similar size, their total specific angular momentum within the virial radius,  $R_{\text{vir}}(z)$ , was averaged in order to give a statistical representation of the growth of  $J/M$  with redshift. The evolutions of the mean specific angular momentum for the gas and dark matter are shown in Fig. 11. The TREESPH and GRAPESPH results are plotted as solid and dashed lines respectively, and are almost identical. The specific angular momenta of the dark matter and gas have very similar values, but at late times the specific angular momentum of the gas component exceeds that of the dark matter. This is because  $J/M$  of both the components increases with radius. Consequently, when the central, low  $J/M$ , gas turns into stars, the specific angular momentum of the remaining gas within the virial radius is enhanced.

Fig. 12 shows the radial specific angular momentum profiles of the stellar components in each halo for both TREESPH and GRAPESPH simulations at three different epochs. The redshifts for TREESPH results are  $z = 0.63$  (dotted lines),  $0.30$  (dashed lines), and  $0.0$  (solid lines); for GRAPESPH, the first redshift is  $z = 0.68$ . It can be inferred from the large number of almost horizontal lines with the occasional vertical jump, that the dominant stellar concentrations are usually well isolated from other star particles. The two most disc-like final stellar components, belonging to Haloes 2 and 5, evolve relatively steadily from  $z = 0.6$  to the present, whilst the remaining haloes suffer more interactions with other stellar clumps. The differences in the positions and sizes of the vertical jumps in  $J/M$  in identical halos run with TREESPH and GRAPESPH are caused by the evolutionary differences identified in Section 5.2.1 that lead to sub-condensations in each code with different orbits.

The morphology and specific angular momenta of the final stellar objects appear to be sensitive to the merger histories undergone by the parent haloes. This point has been investigated quantitatively by resimulating two haloes with the cooling switched on at  $z_{\text{cool}} = 4$  and  $z_{\text{cool}} = 0.6$ , in addition to the usual  $z_{\text{cool}} = 1$ . The evolution of the stellar  $J/M$  measured within the central 20 kpc is shown in Fig. 13. The top frame shows GRAPESPH results for Halo 2; the bottom frame shows TREESPH results for Halo 5. For Halo 2, it is clear that a significant increase in the final specific angular momentum occurs when the gas is prevented from cooling at early times. The same result is reproduced by the Halo 5 simulations, but only for the change of  $z_{\text{cool}}$  from 4 to 1. This halo evolves very little after  $z = 1$  (see Table 1); the result of suppressing cooling until  $z_{\text{cool}} = 0.6$  is to form a very similar stellar disc as in the  $z_{\text{cool}} = 1$  simulation, but at a slightly later time. From  $z = 1$  to the present, Halo 5 increases its virial mass by a factor of  $\sim 1.5$  whereas Halo 2 grows by a factor of  $\sim 1.2$ . The other three haloes nearly double in mass during this period.

Fig. 14 shows the specific angular momenta of all the three components (stars at 20 kpc, gas and dark matter at the virial radius) for both TREESPH (filled symbols) and GRAPESPH (open symbols) haloes at redshift zero. The circular speed of the haloes is computed from equation (1) with  $R_c$  set to the virial radius  $R_{\text{vir}}$ . Concentrating on the stellar components (plotted as 4-pointed stars for  $z_{\text{cool}} = 4$ , 5-pointed stars for  $z_{\text{cool}} = 1$  and 6-pointed stars for  $z_{\text{cool}} = 0.6$ ), it can be seen that, even allowing for the differences between the two codes, there is a tendency for the more slowly evolving haloes (numbers 2 and 5) to give rise to more rapidly rotating stellar objects, *provided cooling is suppressed at high redshift*. If cooling is allowed to begin at  $z_{\text{cool}} = 4$ , the stellar systems that form in these haloes experience the ‘angular-momentum catastrophe’ seen in previous numerical simulations. The crosses in Fig. 14 show the specific angular momenta of the stars for the Halo 2 TREESPH simulations in which cooling was suppressed using the empirical formula  $g(z)$  of equation (19). The lower cross is for  $z_c = 4$  and the upper cross is for  $z_c = 1$ . The specific angular momentum of the  $z_c = 1$  simulation is an order of magnitude larger than the  $z_c = 4$  run, though it is not as high as in the simulation with cooling abruptly truncated at  $z_{\text{cool}} = 1$ . Nevertheless, these simulations demonstrate

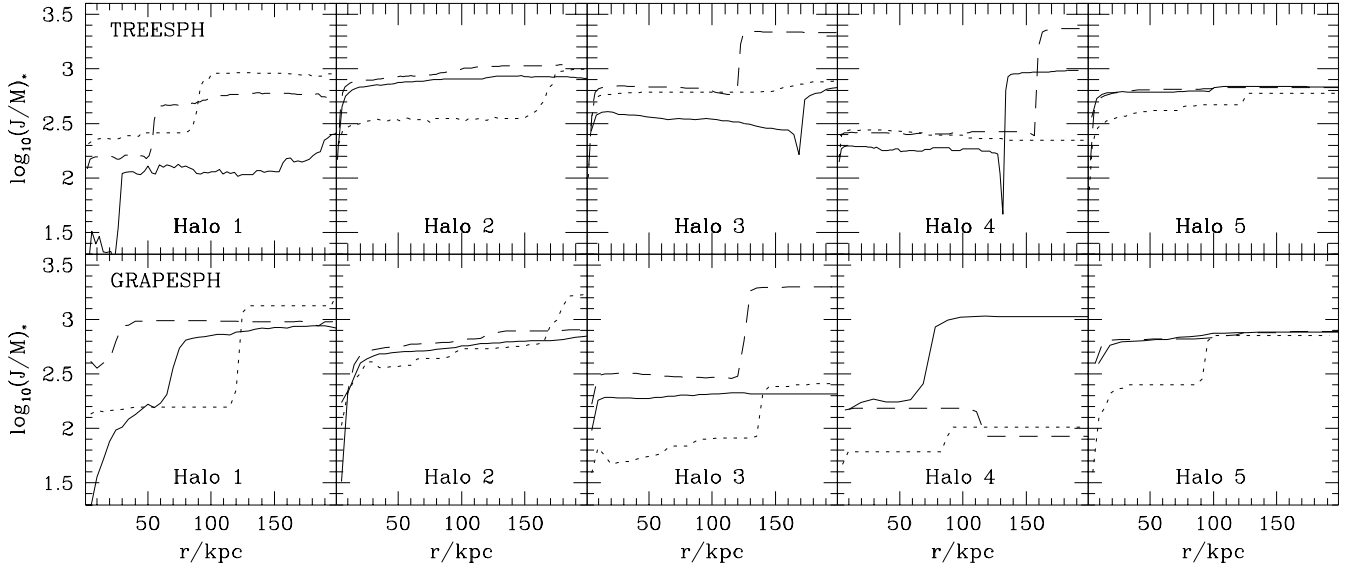


**Figure 12.** Radial specific angular momentum profiles of the stellar components in each halo for the simulations with  $z_{\text{cool}} = 1$ . Redshifts for TREESPH results are  $z = 0.63$  (dotted lines), 0.30 (dashed lines), and 0.0 (solid lines); redshifts for GRAPESPH results are similar except that the first redshift is  $z = 0.68$ .

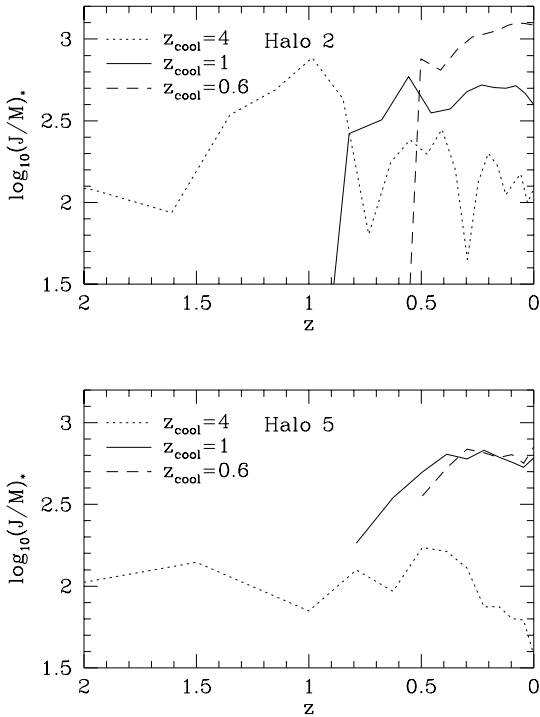


**Figure 13.** Evolution of the stellar  $J/M$  measured within the central 20kpc for GRAPESPH Halo 2 and TREESPH Halo 5.

again the sensitivity of angular momentum evolution to the cooling history.

The solid line in Fig. 14 shows equation 5. The specific angular momenta of the dark matter haloes all lie below this line. This is expected because, as described in Section 4.1, our selection criteria bias against haloes with final spin-

parameters larger than  $\lambda = 0.05$ . All of our haloes therefore have spin parameters less than or equal to the median value of  $\lambda$  measured in N-body simulations (see Figure 1) and hence lie below the line plotted in Fig. 14.

The gas components generally have higher final specific angular momenta than their dark matter haloes. As explained at the start of this subsection, this is because the lower-angular momentum gas in the central regions of the haloes is efficiently converted into stars, leaving an extended atmosphere of high angular momentum gas.

There is good agreement between the TREESPH and GRAPESPH runs plotted in Fig. 14, with one exception, namely the final specific angular momentum of the stellar components of the halo 3 runs with  $z_{\text{cool}} = 1$  (see Section 5.2.1, for a detailed discussion). The general conclusion from both the TREESPH and GRAPESPH simulations is the same however: the stellar systems that form in simulations with high redshift cooling experience an ‘angular-momentum catastrophe’ and end up with specific angular momenta that are between one or two orders of magnitude smaller than the specific angular momenta of real disc galaxies. In contrast, if cooling is suppressed until  $z_{\text{cool}} \sim 1$ , stellar discs can form with angular momenta that are within the range observed for real galaxies. For example, comparing the  $z_{\text{cool}} = 1$  results plotted in Fig. 14 with the results of Figure 1 shows that the stellar systems that form in haloes 5, 3 (in the TREESPH run) and 2 have similar specific angular momenta to real disc galaxies. They also have smaller specific angular momenta, by a factor of about 4, compared to their parent dark matter haloes at  $z = 0$ , in agreement with the results plotted in Figure 1. These results provide powerful evidence that late disc formation is essential if we are to explain their angular momenta.

However, suppressing cooling until  $z_{\text{cool}} = 1$  does not guarantee that disc systems will form by the present day. Thus, even with cooling suppressed until such a recent

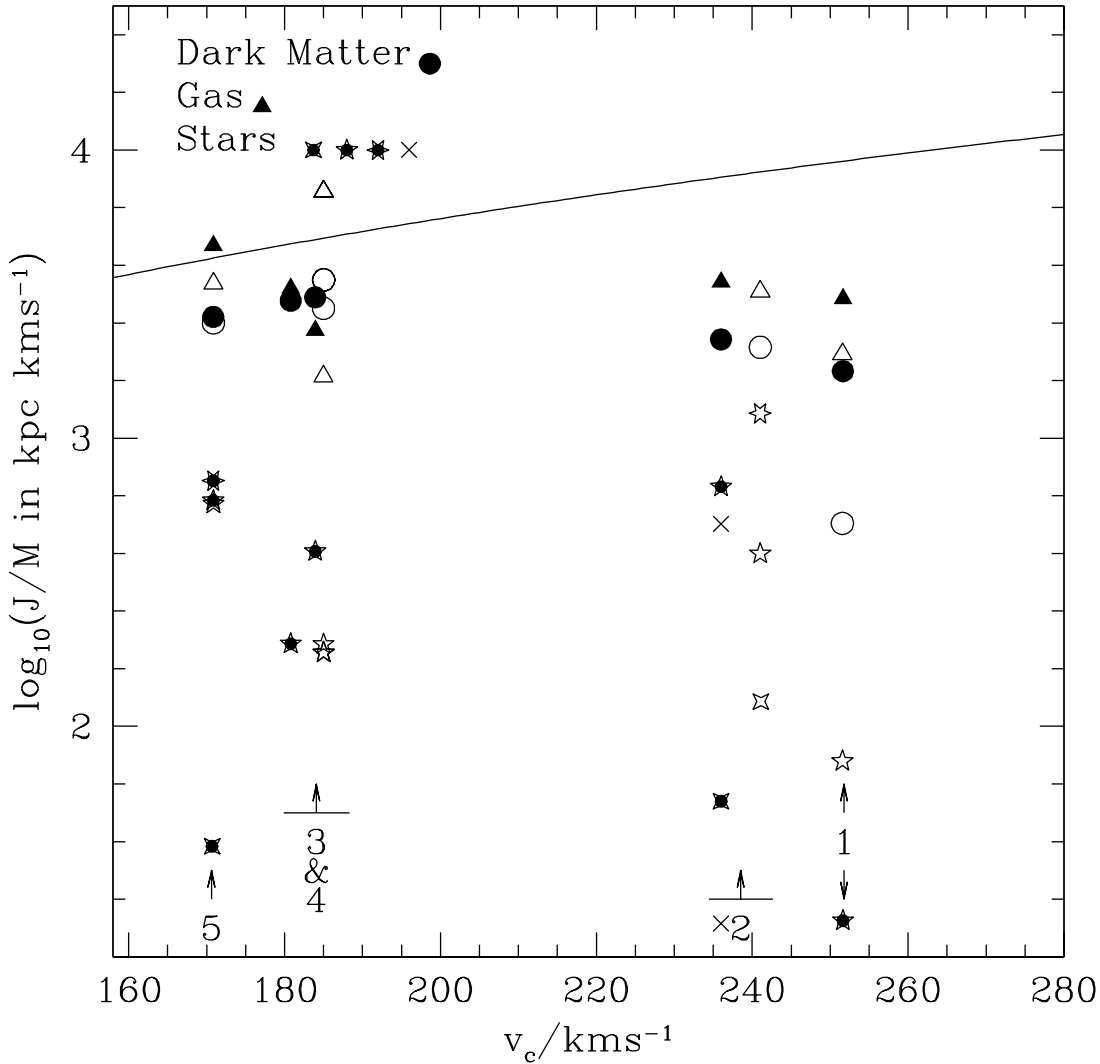


**Figure 14.** Specific angular momenta at  $z = 0$  versus circular speed  $v_c$  for stars within 20 kpc (plotted as stars) gas (plotted as triangles) and dark matter (plotted as circles) at the virial radius. TREESPH results are shown by the filled symbols and GRAPESPH results by the open symbols. For the stellar components, 4–pointed stars show results for runs with  $z_{\text{cool}} = 4$ , 5–pointed stars for  $z_{\text{cool}} = 1$ , and 6–pointed stars for  $z_{\text{cool}} = 0.6$ . Crosses are for Halo 2 stars evolved with cooling suppressed by  $g(z)$ . The abscissa is the circular velocity of the halo at the virial radius. The solid line is equation 5.

epoch, the stellar remnants that form in Haloes 1, 4 (and Halo 3 in the GRAPESPH run) have much lower specific angular momenta than real disc galaxies. This is because these dark matter haloes evolve considerably between  $z = 1$  and the present (nearly doubling their masses within the virial radius); star formation in these haloes occurs in sub-units which merge between  $z = 1$  and the present day, losing angular momentum in the process. The formation of discs thus depends sensitively on the internal structure and merger history of their parent dark matter haloes at recent epochs.

#### 5.4 Colour Evolution

The star formation histories for the five models with  $z_{\text{cool}} = 1$  are shown in Fig. 15. As explained in Section 5.2.2, the star formation histories in the TREESPH and GRAPESPH

runs are slightly different, with more net star formation in the TREESPH models. However, in both sets of models, the star-formation histories are quite well approximated by the form

$$M_*(t') = \alpha(1 - \exp(-\beta t')), \quad (20)$$

with values of  $\alpha$  and  $\beta$  as listed in Fig. 15. In equation 20,  $t'$  denotes the time measured from  $z = 1$  when cooling is switched on. In these models, there is no star formation by construction at  $z > 1$ , and so the entire present day galaxy forms since  $z = 1$ . The star formation rates decline once star formation begins. In the extreme cases shown in Fig. 15, the star formation rates vary between  $\dot{M} \approx 70M_\odot/\text{yr}$  at  $z = 1$  to  $\dot{M} \approx 12M_\odot/\text{yr}$  at  $z = 0$  for Halo 1 (which does not form a final disc) and  $\dot{M} \approx 28M_\odot/\text{yr}$  at  $z = 1$  and  $\dot{M} \approx 1.5M_\odot/\text{yr}$  at  $z = 0$  for Halo 5 (which does form a stellar disc).



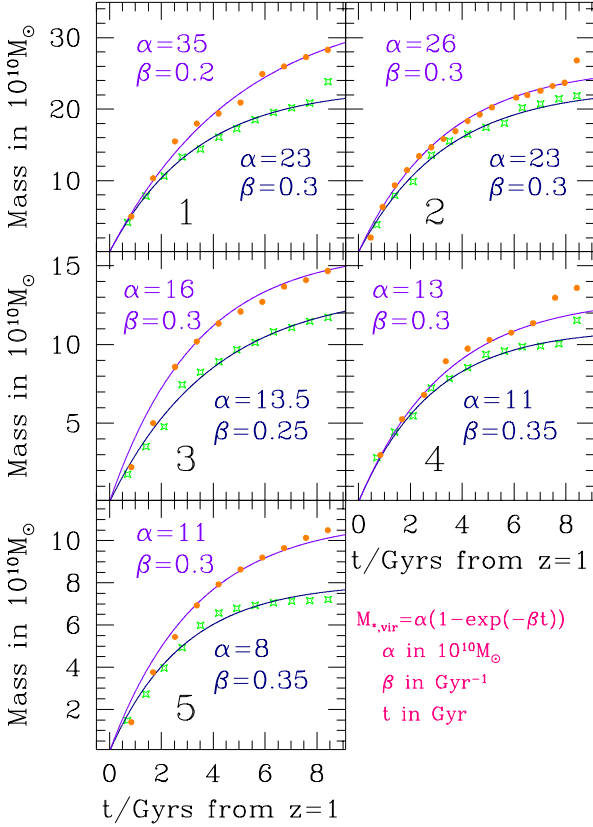


**Figure 15.** Star formation histories for the haloes evolved with  $z_{\text{cool}} = 1$ . The TREESPH runs are shown as the filled circles and the GRAPESPH runs are shown as the open stars. The halo numbers are listed in each panel. The solid lines show fits of equation 20 with values of  $\alpha$  and  $\beta$  as given in each panel.

In the previous subsection, we have argued that high angular momenta of disc galaxies requires that they formed at late epochs. Thus, the question arises as to whether such extreme evolution as implied by Fig. 15 could be compatible with observations of disc galaxies at redshifts  $z \sim 0.5-1$  (Lilly *et al.* 1997, Vogt *et al.* 1997a, b). We have therefore computed the rest frame absolute magnitudes and colours for Haloes 1 and 5 (spanning the range of star formation histories plotted in Fig. 15) using the Bruzual and Charlot (1993) population synthesis code. The results are plotted in Fig. 16 for a Salpeter (1955) initial stellar mass function extending from  $0.1M_{\odot}$  to  $125M_{\odot}$ . These models show that there is weak evolution in the K-band, once star formation is underway. The rest-frame B-band absolute magnitudes brighten by more than a magnitude between  $z = 0$  and  $z = 0.8$ , despite the fact that the stellar disc mass decreases by an order of magnitude between these epochs. This is not surprising because the luminosity, especially in the B-band, is sensitive to the net star-formation rate at early times rather than the underlying disc mass.

An analysis of recent observations of disc evolution (Mao, Mo and White 1998), suggests that at fixed circular speed, discs show very little evolution in B-band luminosity. Comparison with Fig. 16 suggests that the star formation rates in our simulations are probably too high at early

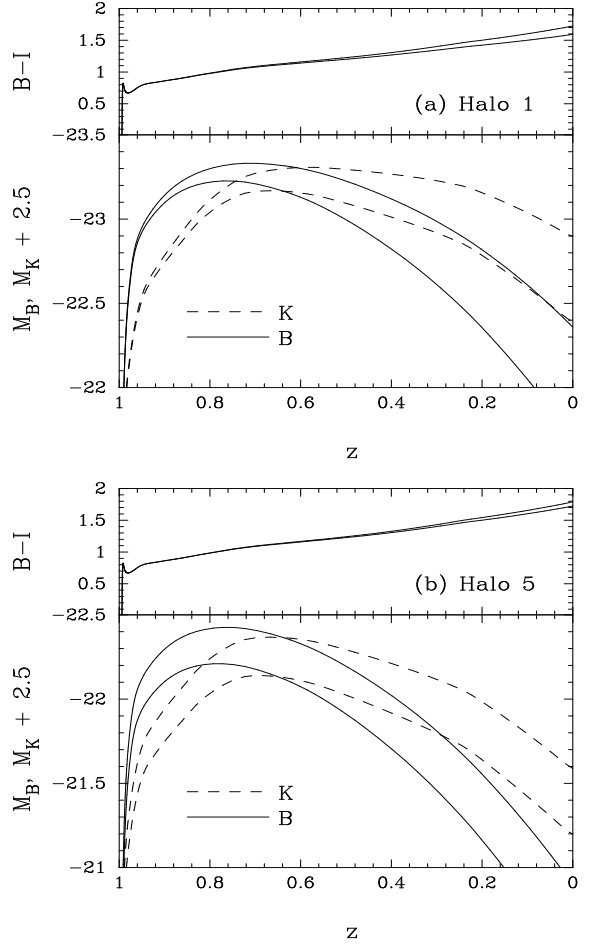


**Figure 16.** Bruzual and Charlot models of the rest-frame absolute magnitude evolution in the  $B$  and  $K$  bands, and  $B - I$  colours, for the star formation rates in Haloes 1 and 5 as plotted in Figure 15. The pairs of lines show the evolution determined for the star formation rates from the TREESPH and GRAPESPH simulations. A standard Salpeter (1955) stellar initial mass function was assumed.

times. In the simple cooling scheme adopted in our models, a reservoir of high density gas builds up in the central regions of the haloes that cools within a dynamical time and forms stars once cooling is switched on. It is therefore likely that the star formation rates will be less strongly peaked to high redshifts in more realistic feedback models and hence that the luminosity evolution will be even weaker than that shown in Fig. 16.

The very strong evolution of disc masses with redshift should manifest itself as a strong evolution of the disc structural parameters (scale lengths) with redshift. Discs at high redshift should have smaller scale lengths than at the present day. However, the gravitational softenings in our simulations are comparable to the disc scale lengths and so we cannot reliably predict either their size or how they will evolve with redshift. (In most of our runs, the stellar disc half-mass radii are about equal to the stellar softening and stay roughly constant as the discs evolve.) Nevertheless, Mao *et al.* (1998) find evidence that at fixed circular speed, disc scale lengths

do decrease as  $(1+z)^{-1}$ . This is compatible both with simple analytical models of disc evolution (*e.g.* Mo *et al.* 1998) and with the conclusions in favour of late disc formation presented in this paper.

## 6 CONCLUSIONS

The purpose of this study has been to investigate whether disc galaxies can form in a CDM universe with angular momenta and sizes similar to those of real disc systems. We have computed the specific angular momenta of CDM haloes from an N-body simulation and compared them with estimates for a large sample of disc galaxies. This comparison shows that disc galaxies have very nearly the same specific angular momenta as those within the virialized region of CDM haloes at  $z \approx 1$ . We therefore conclude that in a CDM-like model, the gas that formed the disc component must have collapsed at recent epochs, very nearly conserving its angular momentum during collapse. This picture is capable of explaining the present day sizes and distribution of surface brightnesses of disc galaxies (see also Dalcanton *et al.* 1997, and Mo *et al.* 1998).

However, numerical simulations of disc formation have shown that the gas experiences an ‘angular momentum catastrophe’ if it is allowed to collapse early (*e.g.* Navarro & Benz, 1991; Navarro, Frenk & White, 1995a; Navarro & Steinmetz 1997). In the absence of feedback processes, the gas collapses into subunits at high redshift, which subsequently merge losing most of their angular momentum to the dark halo material. The specific angular momenta of the resulting gaseous discs are typically two orders of magnitude smaller than those of real disc galaxies.

In this paper, we have tested whether the ‘angular momentum catastrophe’ can be avoided if feedback processes prevent the gas from collapsing until late epochs when haloes are reasonably smooth and slowly evolving. If this can be achieved, it may be possible for the gas to conserve most of its angular momentum during disc formation, as assumed in the simple analytical models of Fall and Efstathiou (1980) and others. We have not attempted to model feedback in any detail in this paper, but have instead suppressed cooling until a specified redshift. We have selected five haloes with present day circular speeds in the range  $150 \lesssim v_c \lesssim 270$  km/s from a dissipationless N-body simulation of an  $\Omega = 1$  CDM model. We have generated higher resolution multi-mass initial conditions of these haloes which we have evolved with two SPH codes, TREESPH and GRAPESPH, that include star formation.

The results from the two codes are generally in good agreement. Most of the differences are caused by the larger softening length of the stellar component of the GRAPESPH code which affects the internal structure of the collapsed objects and their susceptibility to disruption by mergers. In one pair of simulations (runs 11 and 12) the final stellar system has a different morphological appearance in the two codes, appearing disc-like in TREESPH and spheroidal in GRAPESPH. However, in all other simulations, the morphologies of the final stellar systems are qualitatively similar in the two codes.

All of the runs with cooling suppressed until  $z_{\text{cool}} = 4$  produced spheroidal systems with final specific angular mo-

menta of between one and two orders of magnitude lower than their dark matter haloes. These systems experience the ‘angular momentum catastrophe’ seen in previous simulations. However, in the simulations with cooling suppressed until  $z_{\text{cool}} = 1$ , stellar discs can form with specific angular momenta similar to those of real disc galaxies. This occurs in three out of five haloes simulated with TREESPH and two out of five simulated with GRAPESPH. Suppressing disc formation until late epochs can therefore solve the ‘angular momentum catastrophe’ in some cases, but does not guarantee that a disc will survive to the present day. The morphology of the final stellar object in the simulations depends sensitively on the merging history of the parent halo. All of the haloes that we have simulated have been chosen so that they do not merge with a comparable mass system at  $z \lesssim 1$ . Nevertheless, Haloes 1 and 4, approximately double their mass between  $z = 1$  and  $z = 0$  through a succession of mergers and do not maintain stellar discs to the present day. Haloes 2 and 5 grow least between  $z = 1$  and  $z = 0$  (see Table 1) and these produce the most convincing stellar discs in our simulations.

Our simulations have demonstrated that angular momentum evolution during galaxy formation is extremely sensitive to the thermal history of the gas. This suggests that feedback processes can solve the ‘angular momentum catastrophe’ and are a necessary ingredient in disc galaxy formation. The structure of dark matter haloes is also important in determining the angular momentum evolution. In fact, a number of authors (Katz & Gunn, 1991, Vedel *et al.*, 1994, Steinmetz & Muller, 1995, Contardo, Steinmetz and Fritzev von Alvensleben 1998) have shown that gas approximately conserves its angular momentum if it collapses within nearly uniform dark matter haloes that grow by monolithic collapse rather than hierarchical merging. This is not a realistic solution, however, within the context of CDM-like theories. The detailed evolution of dark matter haloes in CDM models will depend on the cosmology and spectrum of fluctuations and these may be important in determining the fraction of disc galaxies at the present day. To address this issue in an unbiased fashion would require a random choice of haloes to be resimulated, unlike that adopted here.

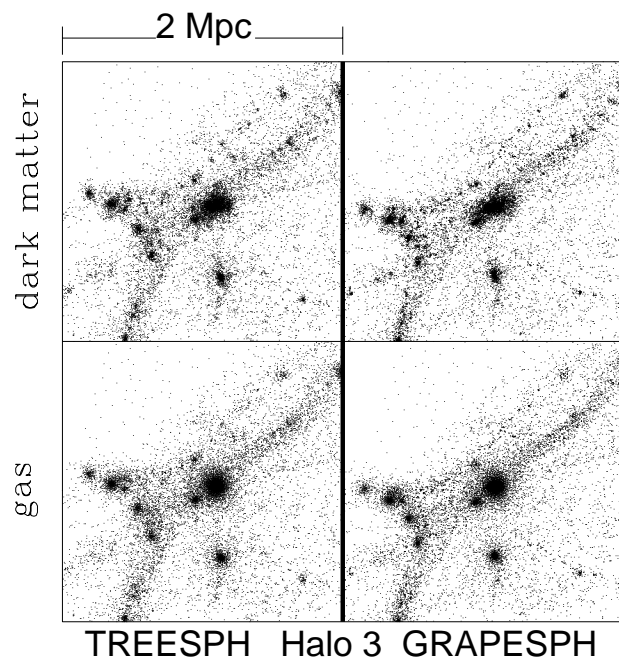
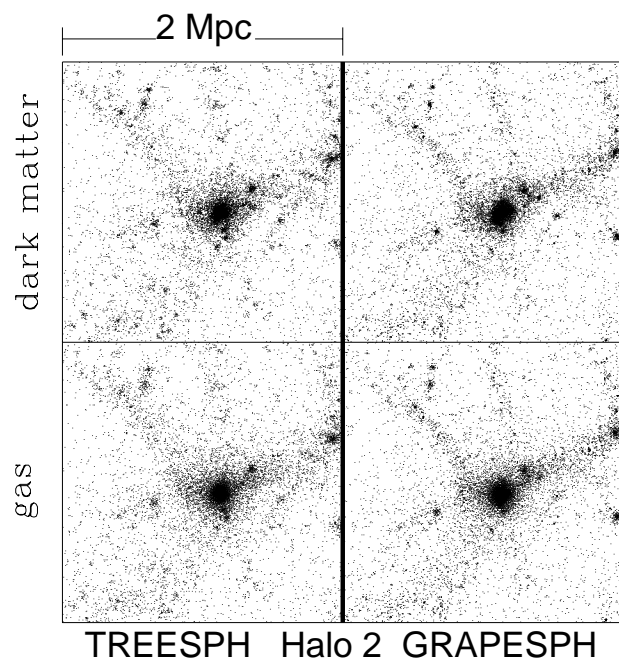
Our simulations suggest that the disc components of galaxies formed at recent epochs, perhaps as late as  $z \lesssim 1$ . This is in qualitative agreement with recent observations showing that discs are evolving significantly over this redshift range (Mao *et al.* 1998). A more detailed comparison with observations will, however, require higher resolution simulations and more realistic models of feedback and star formation.

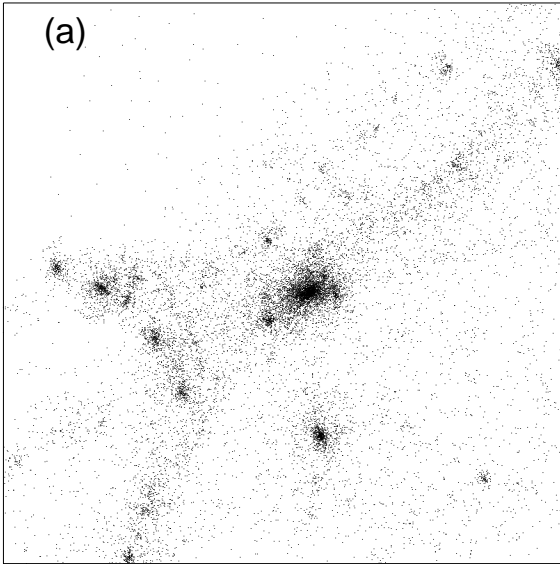
## ACKNOWLEDGMENTS

We thank Yong-Ik Byun and Ken Freeman for allowing us to use their disc photometry parameters prior to publication. MLW acknowledges funding by a PPARC postdoctoral position at the University of Oxford. VRE acknowledges Douglas Heggie for looking after the GRAPE in Edinburgh and the support of a PPARC postdoctoral fellowship. GPE thanks PPARC for the award of a Senior Fellowship.

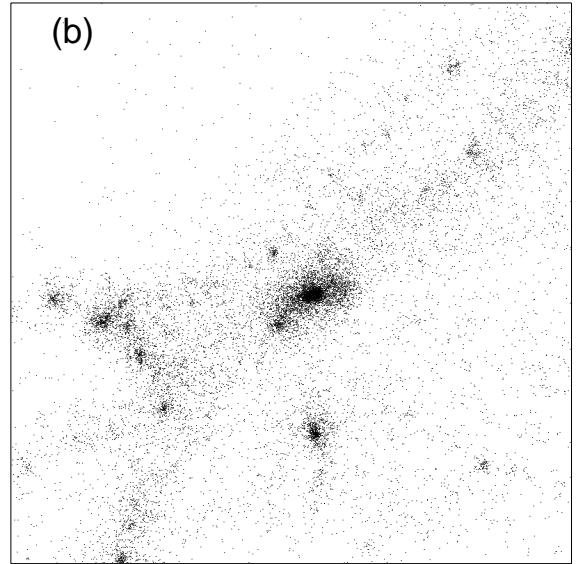
## REFERENCES

- Allen R.J., Shu F.H., 1979, ApJ, 227, 67
- Barnes J., Efstathiou G., 1987, ApJ, 319, 575
- Benz W., Bowers R.L., Cameron A.G.W., Press W.H., 1990, ApJ, 348, 647
- Black J.H., 1981, MNRAS, 197, 553
- Bruzual G., Charlot S., 1993, ApJ, 415, 580
- Byun Y.I., Freeman K.C., 1995, ApJ, 448, 563
- Cen R., 1992, ApJS, 78, 341
- Contardo G., Steinmetz M., Fritze-von Alvensleben U., 1998, ApJ, submitted (astro-ph/9801278)
- Dalcanton J.J., Spergel S.N., Summers F.J., 1997, ApJ, 482, 669
- Davis M., Efstathiou G., Frenk C.S., White S.D.M., 1985, ApJ, 292, 371
- Disney M.J., 1976, Nature, 263, 573
- Efstathiou G., 1995, MNRAS, 272, L25
- Efstathiou G., Davis M., Frenk C.S., White S.D.M., 1985, ApJS, 57, 241
- Efstathiou G., Ellis R.S., Peterson B.A., 1988, MNRAS, 232, 431
- Efstathiou G., Barnes J., 1984, in Formation and evolution of galaxies and large structures in the universe. D. Reidel, Dordrecht, p. 361
- Efstathiou G., Bond J.R., White S.D.M., 1992, MNRAS, 258, L1
- Eke V.R., Cole S., Frenk C.S., 1996, MNRAS, 282, 263
- Eke V.R., Navarro J.F., Frenk C.S., 1998, ApJ, in press (astro-ph/9708070)
- Ewell M.W., 1988, Ph.D. thesis, Princeton University
- Fall S.M., 1983, in *Internal Kinematics and Dynamics of Galaxies*, ed. E. Athanassoula, (Dordrecht: Reidel), p 391.
- Fall S.M., Efstathiou G., 1980, MNRAS, 193, 189
- Frenk C.S., White S.D.M., Davis M., Efstathiou G., 1988, ApJ, 327, 507
- Gingold R.A., Monaghan J.J., 1977, MNRAS, 181, 375
- Gunn J.E., 1982, in *Astrophysical Cosmology*, ed. H.A. Bruck, G. Coyne and M.S. Longair, (Vatican Pontificia Academia Scientiarum), 191.
- Hernquist L., Katz N., 1989, ApJS, 70, 419
- Jenkins A.R. *et al.* 1998, ApJ, in press (astro-ph/9709010)
- Katz N., 1992, ApJ, 391, 502
- Katz N., Gunn J.E., 1991, ApJ, 377, 365
- Katz N., White S.D.M., 1993, ApJ, 412, 455
- Lemson G., Kauffmann, G., 1997, MNRAS submitted, (astro-ph/9710125)
- Lilly S.J., *et al.*, 1997, (astro-ph/9712061)
- Lucy L., 1977, AJ, 82, 1013
- Mao S., Mo H.J., White S.D.M., 1998, submitted to MNRAS, (astro-ph/9712167)
- Mathewson D.S., Ford V.L., Buchhorn M., 1992, ApJS, 81, 413
- Mo H.J., Mao S., White S.D.M., 1998, submitted to MNRAS, (astro-ph/9707344)
- Monaghan J.J., Lattanzio J.C., 1985, A&A, 149, 135
- Navarro J.F., Benz W., 1991, ApJ, 380, 320
- Navarro J.F., White S.D.M., 1993, MNRAS, 265, 271 (NW)
- Navarro J.F., Frenk C.S., White S.D.M., 1995a, MNRAS, 275, 56
- Navarro J.F., Frenk C.S., White S.D.M., 1995b, MNRAS, 275, 720
- Navarro J.F., Frenk C.S., White S.D.M., 1997, ApJ, 490, 493
- Navarro J.F., Steinmetz M., 1997, ApJ, 478, 13
- Okumura S.K., Makino J., Ebisuzaki T., Ito T., Fukushige T., Sugimoto D., 1993, PASJ, 45, 329
- Peebles P.J.E. 1969, ApJ, 155, 393.
- Phillipps S., Disney M., 1986, MNRAS, 221, 1039
- Quinn T., Katz N., Efstathiou G., 1996, MNRAS, 278, L49
- Salpeter E.E., 1955, ApJ, 121, 161
- Steinmetz M., 1996, MNRAS, 278, 1005
- Steinmetz M., Muller E., 1995, MNRAS, 276, 549
- Steinmetz M., White S.D.M., 1997, MNRAS, 288, 545
- Sugimoto D., Chikada Y., Makino J., Ito T., Ebisuzaki T., Umemura M., 1990, Nat, 345, 33
- Tully R.B., Fisher J.R., 1977, A&A, 54, 661
- Vedel H., Hellsten U., Sommer-Larsen J., 1994, MNRAS, 271, 743
- Vogt N.P., Forbes D.A., Phillips A.C., Gronwall C., Faber S.M., Illingworth G.D., Koo D., 1997a, ApJ, 465, L15
- Vogt N.P., Phillips A.C., Faber S.M., Gallego J., Gronwall C., Guzman R., Illingworth G.D., Koo D., Lowenthal J.D., 1997b, ApJ, 479, L121
- White S.D.M., 1984, ApJ, 286, 38
- White S.D.M., Rees M.J., 1978, MNRAS, 183 341.
- White S.D.M., Efstathiou G., Frenk C.S., 1993, MNRAS, 262, 1023
- Yepes G., Kates R., Khokhlov A., Klypin A., 1997, MNRAS, 284, 235
- Zurek W.H., Quinn P.J., Salmon J.K., 1988, ApJ, 330, 519.

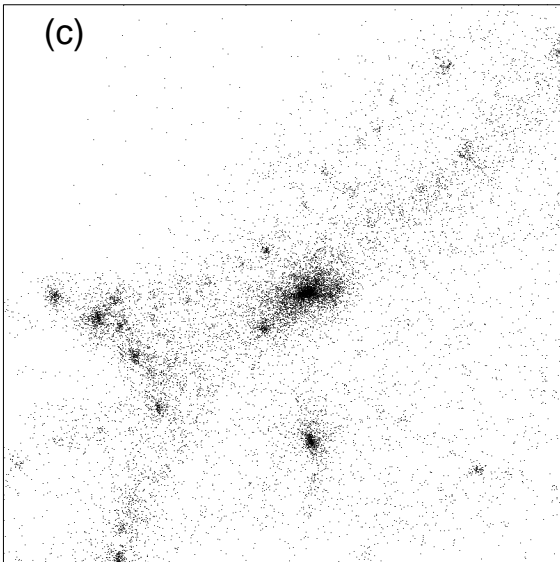




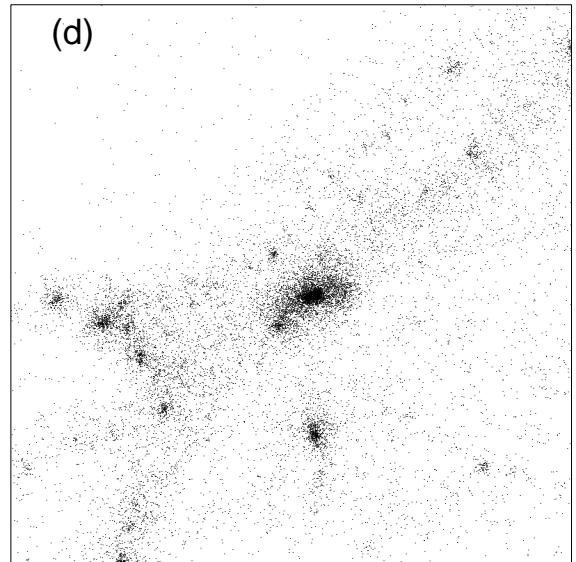
TREESPH Halo 3



GRAPESPH Halo 3



TREESPH Halo 3



GRAPESPH Halo 3